Applied Ocean Research 125 (2022) 103247

Contents lists available at ScienceDirect

Applied Ocean Research

journal homepage: www.elsevier.com/locate/apor

Model tests of a hydroelastic truncated floating bridge

José Miguel Rodrigues *, Thomas Viuff, Ole David Økland

SINTEF Ocean, Postboks 4762 Torgarden, Trondheim 7465, Norway

ARTICLE INFO

Keywords:
Large floating coastal structures
Floating bridges
Hydroelasticity
Model tests
Wave structure interaction
Structural dynamics

ABSTRACT

Literature on tank tests of floating bridges is extremely rare, while a very limited number of publications covering tests of other types of very large floating structures exist. Here, the authors share their experience in designing and carrying out a model test campaign aimed at providing empirical data to aid the process of validating and calibrating a numerically based design of a generic floating bridge. The tested model represents a truncated segment of a full straight bridge at a fjord crossing supported by floating pontoons with 4 mooring clusters providing additional lateral stiffness. The tested environmental conditions comprise combinations of regular and irregular waves, current and wind, including a spectral amplitude inhomogeneous condition realization. The setup of the objectives, strategy adopted for the truncation, experimental setup and relevant system identification and control procedures carried out, are explained thoroughly. Noteworthy is a novel approach for carrying out static pull-outs and decays using a set of actuator winches, also used for applying prescribed wind forces on the model, allowing for inhomogeneous dynamic prescribed forces to be accurately applied.

A dataset of time series and selected video recordings is publicly shared for selected measurements and test runs. It is expected that this paper and the accompanying dataset become a valuable resource for researchers and engineers addressing model testing or experimental validation of numerical models of floating bridges within the functional design process of these structures. Specifically, the dataset should provide important empirical data for benchmarking numerical predictions of hydrodynamic interaction, and hydroelasticity models in general. Recommendations for testing of floating bridges in a basin are also given, based on the experience gathered in the project.

1. Introduction

Permanent floating bridges are engineering solutions that answer to uncommon requirements and constrains to connect two land masses. In general, they address the need to connect heavily populated areas with a very wide and deep body of water in the way; or where extremely soft bottom soil is present, therefore prohibiting conventional pier supported solutions. In addition, the environmental criteria to allow for floating bridges efficiency and safety prohibits their implementation in areas with very strong winds or waves. These two considerations may constitute the main causes for the reduced number of permanent large floating bridges in the world today – see Kvåle (2017) for a full list of floating bridges in operation. On the other hand, these conditions are exceptionally met in Norway. In fact, floating bridges are being considered for several Fjord crossings due to bottom depths reaching as high as 500m, while two have already been built and are under operation: Bergsøysund Bridge in Møre og Romsdal, and the Nordhordland Bridge (Salhus Bridge) in Hordaland.

1.1. Challenges in floating bridges design

The Norwegian Public Roads Administration (NPRA) has a long-term goal of building a ferry-free route (E39) connecting the cities of Kristiansand and Trondheim, in Southern and Central Norway, respectively. Large floating bridges are being considered, but the deployment of these structures requires adopting design related procedures for which one can argue that no established solution or general guidelines are truly available to address the following challenges on how to efficiently (Rodrigues et al., 2020):

1 Model current, wave, and wind, inhomogeneous environmental loads over the structure.
2 Predict the hydroelastic behaviour of large floating coastal structures (LFCS) under these inhomogeneous conditions.

* Corresponding author.
E-mail address: miguel.rodrigues@sintef.no (J.M. Rodrigues).

https://doi.org/10.1016/j.apor.2022.103247
Received 30 March 2022; Accepted 6 June 2022
Available online 11 June 2022

Fig. 1. Hydroelastic bridge model at MARINTEK [Xiang and Løken, 2019].

3 Design station-keeping systems for large flexible floating structures, e.g. moorings.
4 Model hydroelastic effects in combinations with articulated/elastic interconnections between structural parts.

Given these challenges, an important part of the design development for LFCS is to carry out physical tests with a scaled model in a controlled environment within a qualification assessment phase.

The problem with performing such type of tests is the very large extension of these bridges, which can be in the order of 5 km in full scale. This means that modelling of the full structure would require a scaled model with 50 m length for a scale 1:100. Then, considering the typically small wave heights and peak periods in a Fjord (say 1-2 m and 5 s, respectively, for the 1-year limit condition), waves with significant wave heights of 10 mm must be generated and accurately modelled across a 50 m extension in a basin. Only a limited number of tanks in the world can handle such large models, but there are other important difficulties in addition to the quality of wave generation: (1) hydrodynamic quantities' scaling issues for such a small scale; (2) quality of the model production; (3) quality of the measurements.

To circumvent this problem, the option is to have the full-span structure design, analysis and qualification based solely on numerical models when it comes to the full structure. In fact, several numerical studies addressing floating bridges in fjord crossings have been carried out, typically to predict extreme responses. Some recent examples are the efficient framework for full long-term extreme response analysis for a long-span pontoon bridge subjected to wave loads established by Giske et al. (2018), the study of the effects of wave directionality on extreme response for a long end-anchored floating bridge by Viuff et al. (2019), and the inhomogeneous wave load effects on a floating bridge by Cheng et al. (2018.

The numerical models then need to be calibrated and validated. One option is to resort to physical tests with a scaled portion of the full structure: a truncated bridge. In that case, care needs to be taken such that relevant phenomena are addressed and that the truncated model allows for determining responses in a realistic environment. Obviously, these need to be in line with the specific objectives of the tests and time and budget constraints of the experimental campaign.

1.2. Experimental studies on floating bridges

Published physical scaled model studies on the hydroelastic response of floating bridges to waves, current and wind are close to non-existing. A quite unique experimental campaign was the one at MARINTEK's (presently SINTEF Ocean) ocean basin in 1990 of a curved floating bridge (Xiang and Løken, 2019) – see Fig. 1. The full length of the 8 pontoon bridge (845 m in full scale) was modelled, where each pontoon had 45 m length and 22 m width in full scale. Single pontoon tests were also carried out. Scales of 1:40 and 1:20 for the full bridge and single pontoon tests were used, respectively. The two ends of the model were fixed via universal joints flexible in bending and infinitely stiff in the torsional and longitudinal directions.

Recently, Xiang and Løken (2019) carried out a validation study of their OrcaFlex (ORCINA, 2021) based numerical model using the results of MARINTEK's tests. Excitation loads agreed well while hydro-elastic responses of the structure compared satisfactorily. Hydrodynamic interaction between pontoons was found to be non-negligible and predicted by the numerical code. An important issue was identified in load cases with concurrent waves and current: numerical predictions expected a damping effect of the motions from the current, while experimental data showed an opposite trend. A similar observation was made by Viuff et al. (2020). Xiang and Løken then conclude on the necessity of carrying out further validation work for floating bridges designs with much larger length, in the order of 5 km.

1.3. Experimental studies on other very large floating structures

Considering other types of very large floating structures (VLFS), some important work has been published regarding experimental campaigns. Ohmatsu (2005) provided an overview of numerical estimation and analytical methods for the hydroelastic behaviour of VLFS within the Japanese Mega-float project 1995–2000. Model tests carried out for the Haneda 3 km floating airport concept at a scale of 1:200 are mentioned: the model length was 15 m, the vertical displacement

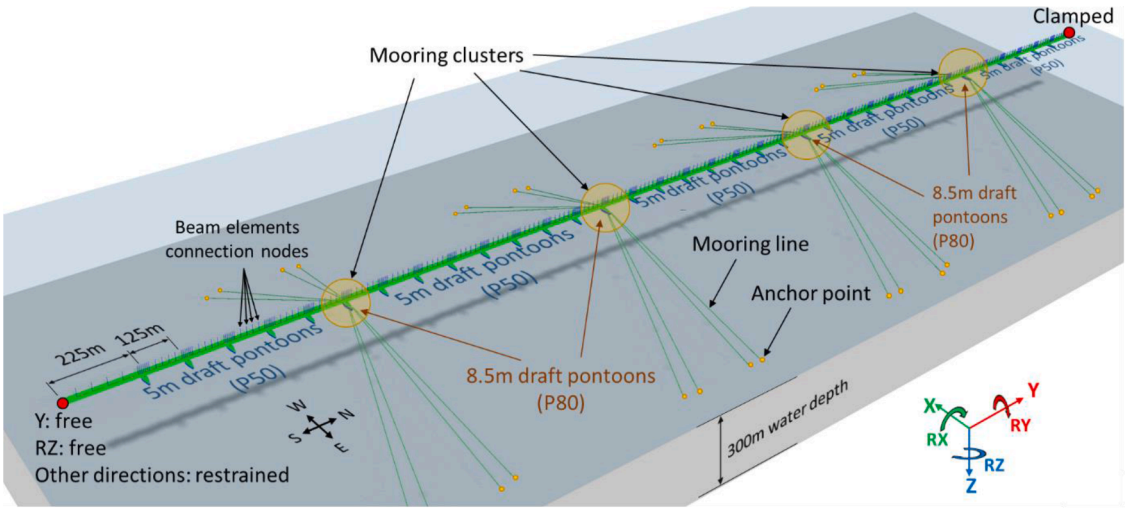

Fig. 2. Numerical model of the generic bridge (end boundary conditions are fixed in all degrees of freedom unless otherwise noted).

measured at 128 points, the structural strain at 32 points, and the mooring force at 4 points.

Kagemoto et al. (1998) proposed a prediction method for the hydro-elastic behaviour of a very large box-shaped flexible structure; the structure being representative of a floating international airport. Experiments were also carried out in a wave tank with an acrylic flexible model, which consisted of 100 (20 × 5) buoyant rectangular solids. Each of the solids was attached to the upper flexible deck. The model was 2 m long, which, if geometrical scaling was adapted, implies a geometrical scaling factor of 2500 for a stated typical real structure length of 5 km. Height and draft dimensions were also not correctly scaled from their full-scale values. The model tests were evidently aimed at a fundamental validation of the proposed numerical model.

Song et al. (2008) performed model tests of a VLFS in a scale of 1:100 to study the effect of inhomogeneity caused by an uneven bottom. Different shoal geometries were set on the bottom of the wave basin. The tests were carried out in regular long crested waves, without wind or current. The water depth, incident wave angle and shoal shape was varied. The results were compared with a coupled and linear hydroelastic numerical model.

Another interesting work is the one by Yoon et al. (2014) who validated their numerical model of a multiple hinge connected VLFS with experiments with a model of 3 m length, 0.6 m width, 4 cm thickness, and a draft of 11 mm. The tests were carried out in regular long crested waves for different heading angles. No wind or current force effects were modelled.

Other published research works worth mentioning briefly are as follows: (a) The series of model tests with various box-type floating breakwaters (Stansberg, 1996, 1990) and the model tests with a large floating hydrocarbon storage facility (Fonseca et al., 2019), all performed at SINTEF Ocean's basin in Trondheim; (b) The experimental hydroelastic analysis of a 8 × 1.2 × 0.074 m^3 floating composite board with end perforated plates emulating a VLFS under the action of waves in Cheng et al. (2016); (c) Already in 2020, MARIN performed tests on a floating mega island composed of square shaped interconnected floating modules within the SPACE@SEA Horizon 2020 European project (MARIN, 2020).

1.4. The present study

LFCS - Design and Verification of Large Floating Coastal Structures was a research project, funded by the Research Council of Norway, focused on producing recommendations for design of large floating coastal structures and developing methods and tools for hydroelastic analysis of coastal structures in spatially inhomogeneous environmental conditions and bathymetry (SINTEF Ocean, 2017). The project was established by SINTEF Ocean and the Norwegian University of Science and Technology (NTNU) with the support of the Norwegian Research Council, the Norwegian Public Roads Administration –*Statens vegvesen*– (NPRA), Hydro ASA, Multiconsult AS, SWECO AS, and LMG Marin AS. The project started in Nov.30, 2017, and finished in the summer of 2021.

In LFCS, focus was mainly set on floating bridges for fjord crossings, underpinned by NPRA's long-term goal of building a ferry-free route (E39) – scaled physical model tests were a major activity in the project. A thorough review of related relevant concepts for fjord crossings (not limited to bridges), their characteristic behaviour and design criteria for serviceability and safety (especially dynamic response due to environmental and accidental loads), with a highlight on development trends, can be found in (Moan and Eidem, 2020). A presentation of the project, and a summary of the related review work on environmental conditions, numerical prediction of loads, structural responses, mooring design and planed physical scaled model tests, is reported in Rodrigues et al. (2020).

Also in Rodrigues et al. (2020), a general overview of the objectives and planned approach to the model tests within the LFCS project was given for a campaign to take place in 2020 targeting validation and calibration of the numerical model of a generic bridge. In August 2020, the tests were carried out at SINTEF Ocean's basin. The tests configured a flexible scale model of a generic floating bridge truncated section in excess of 33m length, supported by 9 pontoons. Tests with regular and irregular waves in different headings, current and wind were carried out, including a run with an inhomogeneous irregular wave. Measurements included 6-degree-of-freedom (dof) motions of the pontoons, 27 3-dof motions at points distributed along the bridge deck, bending and torsional moments and shear forces in way of 4 inter-pontoon spans, mooring forces, absolute and relative free-surface elevation, and wind forces. A particular novel aspect is the deployment of actuator winches pulling wires attached to the model to emulate wind forces distributed along the bridge; with the same system being used to perform *flexible*, easily prescribed, horizontal pull-out and decay tests. The experimental

Table 1
Main characteristics of the generic bridge.

Item	Value
Pontoon spacing	125 m
Distance between moored pontoons	1000 m
Water depth	300 m
No. of pontoons	35
No. of mooring lines per moored pontoon	8

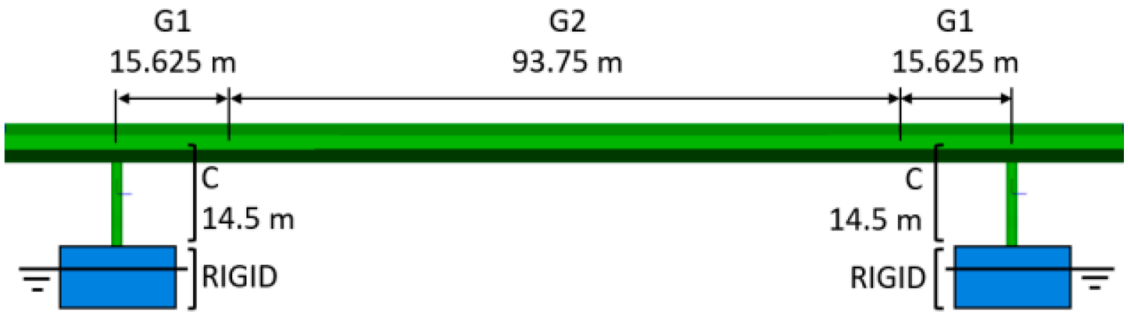

Fig. 3. Composite girder in the generic bridge – G1,G2 and C denote different cross sections.

Table 2
Cross sectional properties of the generic bridge. Iy and Iz are the second moments of area about the horizontal and vertical axis passing through the centroid of the section, respectively. Ix denotes the torsional stiffness factor.

Section	Mass [kg/m]	Ax [m^2]	Ix [m^4]	Iy [m^4]	Iz [m^4]
G2	16 040	1.172	6.649	3.175	89.600
G1	19 780	1.649	7.471	4.014	116.100
C	9 180	1.530	12.940	14.920	9.650

campaign was further supported by the application of a numerical hydroelastic analysis of the model.

In the present paper, the authors share their experience in designing and carrying out the model test campaign, the setup of the objectives, the strategy adopted, the choices taken, and the relevant system identification and control procedures carried out. Proposed guidelines for performing similar physical tests are also presented.

A thorough description of the tests supports a dataset of time series and selected video recordings, which is publicly shared for selected measurements and test runs (Rodrigues, 2022). It is expected that this paper and the accompanying dataset become a valuable resource for researchers addressing floating bridge designs, hydrodynamic interaction, and hydroelasticity in general.

The structure of this paper is as follows. The generic floating bridge, characteristic environment and truncation strategy are described in Section 2. The physical and numerical models of the truncated bridge are the focus of Section 3. The experimental setup and selected test matrix are presented in Section 4, and, in Section 5, the waves and current generation and assessment are described. Section 6 includes selected global results from the campaign and their comparison with the numerical hydroelastic model focusing on model verification. Overall conclusions and recommendations are given in Section 7.

2. Reference bridge, environment, and truncation

2.1. Reference bridge

The study is based on a simplified generic version of the Bjørnafjord floating bridge concept (phase 3) (Statens vegvesen, 2017): a straight side anchored bridge. A simplified numerical aero-hydroelastic model of the floating part of the bridge was made resorting to the software workbench SIMA (SINTEF Ocean, 2021), which allows for the coupled

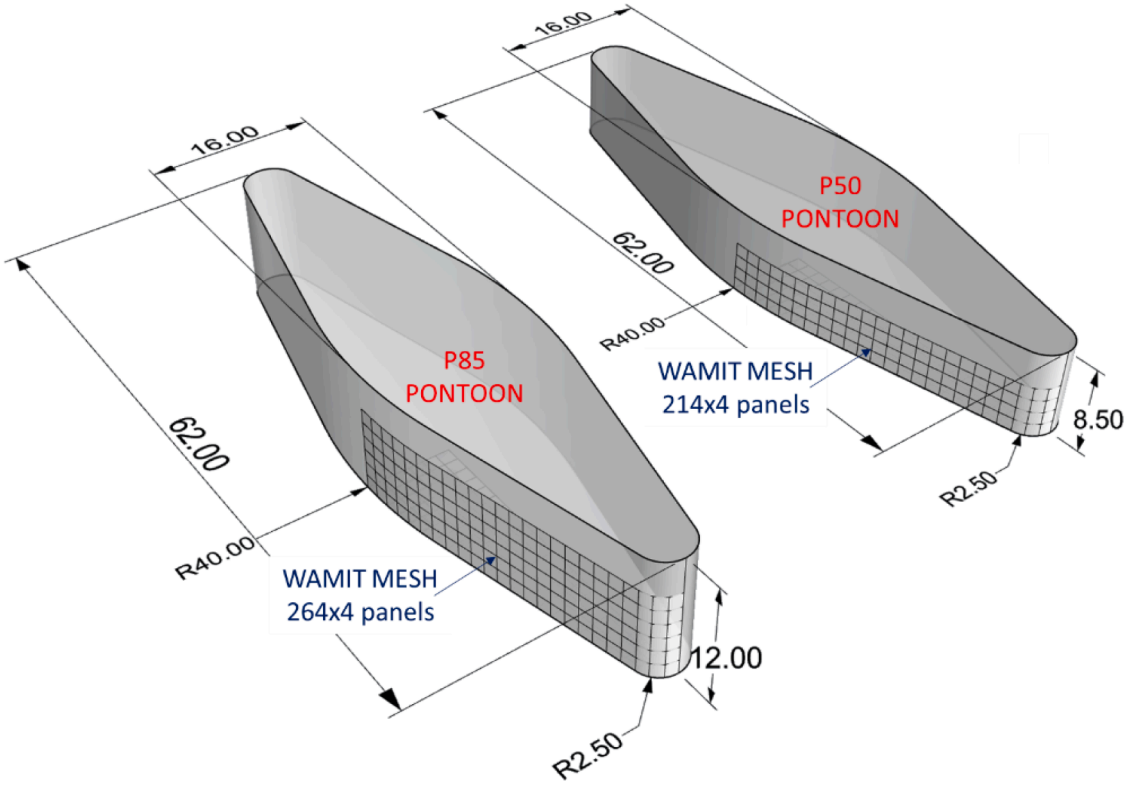

Fig. 4. Geometry and (WAMIT) meshing of the pontoons – dimensions in metres.

Table 3
Geometric characteristics of the pontoons. VCG and VCB stand for vertical centre of gravity and vertical centre of buoyancy, respectively, and are given in relation to the still waterline with positive values in the upward from that reference. C33, C44 and C55 denote the hydrostatic stiffness in the heave, roll and pitch directions, considering local pontoon coordinate systems parallel to the one shown in Fig. 2.

Type	Length [m]	Width [m]	R1 [m]	R2 [m]	Draft [m]	Freeboard [m]	Displacement [tonne]	VCG [m]	VCB [m]	C33 [kN/m]	C44 [kN.m]	C55 [kN.m]
P50	62.0	16.0	40.0	2.5	5.0	3.5	3 421	-0.75	-2.50	6.70×10^3	8.92×10^4	1.47×10^6
P85	62.0	16.0	40.0	2.5	8.5	3.5	5 815	-2.50	-4.25	6.70×10^3	8.92×10^4	1.47×10^6

Table 4
Design environmental conditions for the Bjørnafjord bridge site. H_S and T_P denote significant wave height and wave peak period, respectively.

Case	Return period [years]	Wind sea			Swell			Wind		Current	
		H_S [m]	T_P [s]	Dir (from) [deg]	H_S [m]	T_P [s]	Dir (from) [deg]	Mean speed [m/s]	Dir (from) [deg]	Speed [m/s]	Dir (from) [deg]
DC 1	1	1.6	5.3	90	-	-	-	18.3	100	1	100
DC 2	1	1.5	5.1	335	0.26	20	300	21.5	100	1	280
DC 3	100	2.8	6.6	90	-	-	-	25.1	100	1.4	100
DC 4	100	2.8	6.6	75	-	-	-	25.1	100	1.4	100
DC 5	100	2.5	6.2	335	0.4	20	300	29.5	280	1.4	280
DC 6	100	2.4	5.9	280	0.4	20	300	29.5	280	1.4	280
DC 7	10 000	3.9	7.1	90	-	-	-	25.1	100	1.4	100
DC 8	10 000	3.9	7.1	75	-	-	-	25.1	100	1.4	100
DC 9	10 000	3.5	6.7	335	0.4	20	300	29.5	280	1.4	280
DC 10	10 000	2.7	5.6	190	0.4	20	300	29.5	280	1.4	280

aerodynamic, hydrodynamic, and structural analysis of slender marine structures, including moorings. A coupled-analysis implementation of a time domain simulation tool for study of motions and station keeping of multibody systems (SIMO) with the large displacement slender element finite element method solver (RIFLEX), both part of SIMA, were used. A 3D view of the geometrical representation of the numerical model is shown in Fig. 2. The model tests are targeted at providing relevant empirical data to the validation and calibration of this numerical model.

The generic reference model configures a straight bridge supported by 35 floating pontoons positioned at every 125 m, four of which are fitted with 8 mooring lines providing the bridge lateral stiffness in addition to the boundary conditions at the connections to land. The end boundary conditions are a clamped connection, in the northern side, and a hybrid condition on the southern side. The overall characteristics of the reference model are listed in Table 1.

Three different cross sections for the slender elements are present in the model, which follow the repeating pattern illustrated in Fig. 3 depicting the three main structural elements: pontoons, girder, and

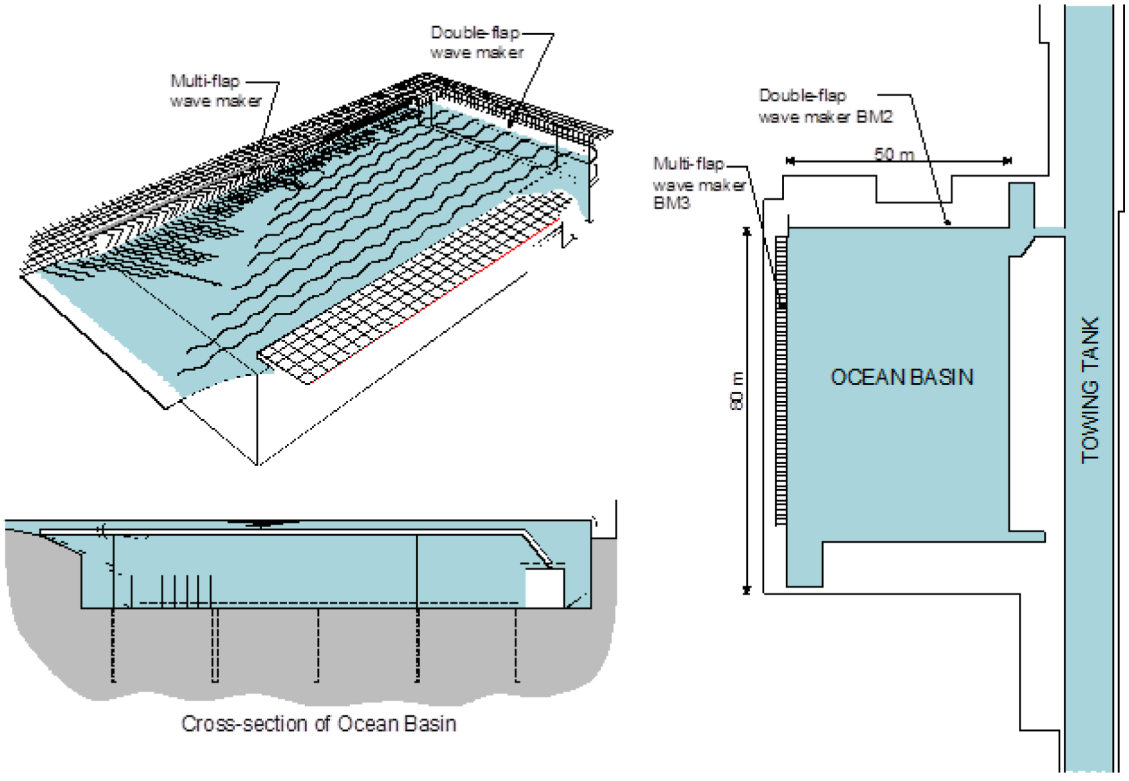

Fig. 5. The Ocean Basin laboratory at SINTEF Ocean.

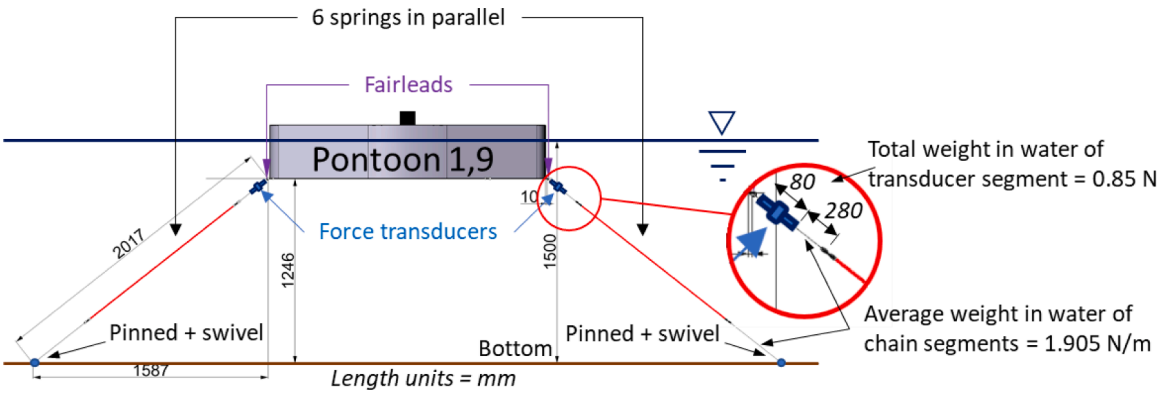

Fig. 6. Mooring geometry in still water in model scale (force transducer not to scale).

columns (which connect the pontoons to the girder). The properties of each cross section are listed in Table 2. The moored pontoons (denoted P85) have a larger draft that the remaining ones (denoted P50), while keeping the same waterplane area and free-board – see Fig. 4. Geometric characteristics of each type of pontoon are listed in Table 3.

2.2. Characteristic environment

Characteristic response values due to environmental loads such as wind and waves should be determined based on a long-term site-specific response analysis. In lieu of these analyses the characteristic response values for wind, wave and current action are determined based on a selection of short-term storm states. Screening of design storms based in Statens vegvesen (2018) was performed and reported in Multiconsult (2017). The obtained design load cases are listed in Table 4. The cases correspond to JONSWAP spectra with peak enhancement factor in the range of 1.8–2.3 and directional spreading with exponent within 4–6 and 10–20, for the wind sea and swell, respectively, considering a cosine spreading model.

It is important to note that these load cases were used as a reference for the experimental campaign presented in this paper, not as a load case list to be strictly followed in the experiments. Wave coverage in the ocean basin, scaling effects in terms of quality of the waves and wave-maker limitations, as well as time and budget constraints, were taken into consideration to arrive at a final load case list, of which a subset is addressed herein.

2.3. Truncation strategy

The experiments were conducted in SINTEF Ocean's Ocean Laboratory at Tyholt, Trondheim, Norway (Fig. 5). The Ocean Laboratory is roughly 50×80 m^2. The depth of the basin is 10.0 m with a floor section with area 48×42 m^2 adjustable from 0.0 to 8.7 m depth. The truncation strategy to cope with the limited size of the basin, among other factors, are described in the following sections.

2.3.1. Scaling

The generic bridge model is 4750 m long, which would lead to a scaled model of 47.5 m length for a scale of 1:100 to be deployed in the ocean basin covering its maximum width. With such a scale, problems related to quality of model production, wave generation, and measurements arise. The strategy adopted was to first investigate the feasible scale range for wave generation in the basin considering long crested versions of the design load cases in Table 4 and applying Fourier scaling. A feasible scale was defined as one for which:

1 The wave-maker limits (amplitude, velocity and acceleration) are not exceeded.
2 Less than 5% of the energy in the wave spectrum tail is cut off due to high-frequency limitations of the wave maker.
3 All spectral ordinates in excess of 10% of the spectral peak are modelled, i.e. can be generated by the wavemaker.
4 Significant wave heights are higher than 2 cm in model scale.
5 Empirical results from the basin's database of wave generation show the feasibility of the targeted sea states, especially considering the lower frequency limits.

A preliminary theoretical screening considering linear waves and neglecting basin effects was carried out for each of the sea-states depicted in Table 4 (wind seas and swell) targeting criteria 1 to 3. It showed that a scale range from 1:20 to 1:40 could be feasible for all sea-states. However, the range was shortened to 1:20–35 as the swell components become unfeasible, when considering criteria 4 and 5. This corroborates (Abrahamsen and Stansberg, 2019) who report that for the typical ranges of significant wave height (H_S) and peak period (T_P) in Table 4, either the swell or the wind sea can typically be modelled – not both.

2.3.2. Truncation length

For the scale range 1:20–1:35 the number of pontoons that could be modelled, considering a conservative maximum model length of 30 m, was 6 to 9. The choice then fell on a scale of 1:33.3, which corresponds to a model with 30 m length (distance from the centres of the first to the last pontoon), including 9 pontoons. The first and last pontoon being moored, one aims at the truncated segment be representative, to some degree, of the central segment between mooring clusters of the reference bridge – see Fig. 2.

2.3.3. Boundary conditions

The boundary conditions at the extremities of the truncated bridge were a particular challenge. Ideally these would enable the truncated segment to behave exactly as if it were part of the full bridge. For this, an active smart 6 DOF force/reacting system deployed at each end of the truncation in the way of the bridge girder ends could be a solution. However, in addition to the considerable development work required, such a system would also need to be calibrated experimentally, thus increasing the complexity even further. Therefore, passive boundary conditions were chosen for the present study, despite its considerable limitations.

Even so, passive boundary conditions are also a challenge in their own. Not only on how they can be deployed in the model tests, but mostly regarding the choice of important phenomena that one wishes to capture in the model tests and how to generate them and capture their effects. Replicating the lowest natural modes of the full bridge is tempting but designing for these directly is problematic, as the "correct" passive boundary conditions depend on the environment loads acting along the full bridge as well as the targeted natural mode. Therefore, a

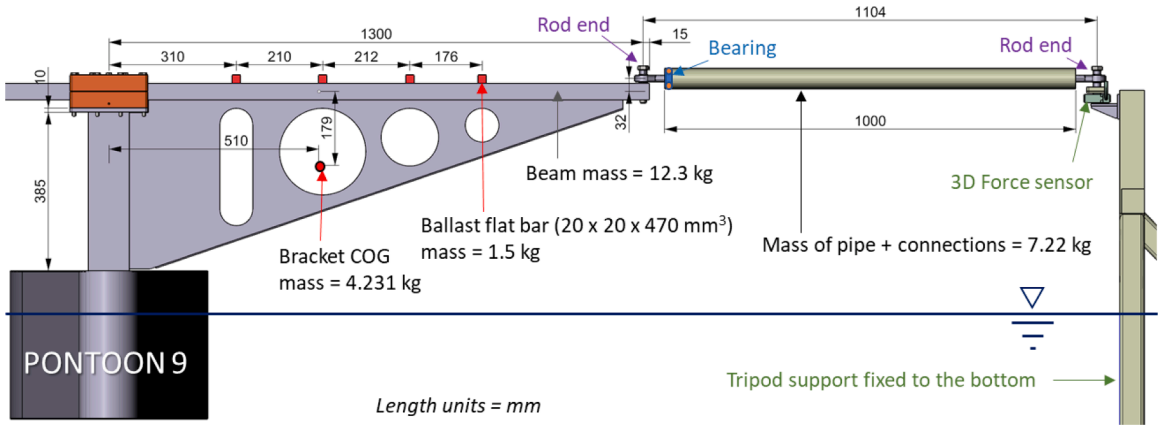

Fig. 7. End beams, with brackets and ballast bars, and connecting pipe at Pontoon 9 extremity (model scale).

simpler approach was adopted: transverse (taut) mooring was applied at the first and last pontoons, i.e. the same positions of the mooring clusters in the full bridge (see Fig. 6), and a light rigid bar with ball joints at each end connecting one side of the truncated segment to a fixed anchor point – see Fig. 7. The mooring stiffness applied at each of the moored pontoons was derived by matching the transverse horizontal restoring of the moored pontoons when subjected to a uniform transverse static load in the 9 pontoons to the deflection of the same pontoons when part of the full bridge subjected to the same transverse uniform static loading in all of its 35 pontoons – see Section 3.2.

Truncation was also performed in the sense of the water depth, as a 300 m water depth would not be possible to model in the basin. Furthermore, the smaller the water depth, the higher the mean speed and quality of the current that can be generated at the basin. A smaller depth also increases the accessibility to the model with obvious time savings for the experimental campaign. A 1.5m depth in model scale (49.95 m in full scale) was chosen, as it exceeded the requirement for consideration of deep water for the wind sea design conditions (wavelength larger than twice the water depth) in Table 4 when using each peak period's corresponding wavelength as a reference value.

3. Truncated model

3.1. Physical model

The 1:33.3 scaled model was built in aluminium, PVC foam, and steel. Nine solid geometrically scaled pontoons were manufactured from Foam-smooth PVC *Divinycell H60* – such a configuration dramatically reduces the problem of watertightness. A 2mm aluminium shell plating was applied to each pontoon's outer surfaces, except for the P85 pontoons. For those, a 5mm steel plate was fitted at their bottom in order to increase the mass and provide a robust support for the fairleads of the mooring lines.

The columns connecting the pontoons to the bridge girder were modelled as rigid square pipes with a top flange to connect to clamps which tighten the inter-span connections of the bridge girder. Each column was built into each pontoon penetrating down to the pontoon's bottom. A layer of epoxy glue was poured into the base of the interior of each column to avoid a weak point regarding watertightness, in otherwise completely solid pontoons. The pontoon-plus-column pairs constitute rigid bodies considering the excitation frequency range in the experiments (numerical simulations with Autodesk Inventor showed that the first vibration mode was nearly 40 Hz in model scale, which is well beyond the typical wave frequency of the load conditions tested). Each pontoon was weighted before and after being afloat for 24 h: differences were found to be negligible (< 1%). Additional air swinging tests were performed to document the inertial properties of one representative P50 and one P85 pontoon. Pontoon plus Column ("P+C") set characteristics are listed in Table 5. Mind that in this table the ballast applied (including final adjustments when the model was freely floating in the basin), the Motion Capture System (MOCAP) targets and supporting frames, and instrumentation, are included in the listed values.

For practical purposes the compounded cross-sectional spans in Fig. 3 were reduced to a uniform equivalent cross-section for the bridge girder segments. The equivalent mass per length and stiffness properties were obtained from applying separate uniform loadings along the bridge in the two transverse directions (vertical and horizontal) and a torque. The equivalent properties were then derived such that resulting deflections and twist angles were the same as for the original design. For

Table 6
Bridge girder cross sectional properties in full scale.

	Area	Mass	Ix	Iy	Iz
Model	3.934 m^2	10 888 kg/m	6.8816 m^4	3.3552 m^4	96.8730 m^4
Generic bridge (Eq.)	1.265 m^2	16 975 kg/m	6.9118	3.3903	95.4257
Difference (bare)	+211.06 %	-35.86 %	-0.44 %	-1.04 %	+1.52 %

Table 5
Pontoon + column (P+C set) inertial characteristics in full scale. (XG,YG,ZG) and (IXX,IYY,IZZ) denote the centre of gravity and inertias; both are referenced to a P+C set local coordinate system with orientations similar to the one shown in Fig. 2 with origin at each of the sets' waterplane centre. M denotes mass.

P+C set	1*	2	3	4*	5	6	7	8	9*
M [t]	3115.10	1305.65	1310.41	1304.47	1305.46	1309.05	1307.05	1317.11	3008.29
XG [m]	1.094	-0.005	-0.009	1.614	0.000	-0.015	-0.004	-0.001	-0.759
YG [m]	-0.105	0.002	0.007	-0.002	0.004	0.001	0.004	-0.001	1.065
ZG [m]	-2.440	-2.160	-2.154	-2.162	-2.281	-2.154	-2.151	-2.181	-2.745
IXX [Mt.m^2]	180.21	56.57	57.33	56.45	52.05	56.77	57.10	57.11	205.39
IYY [Mt.m^2]	476.30	236.62	236.87	231.87	236.13	236.91	236.73	238.53	520.14
IZZ [Mt.m^2]	345.81	221.76	222.87	217.50	222.68	221.12	223.24	224.41	378.81

* Ballast distribution in the x direction adjusted to reduce pontoon's trim.

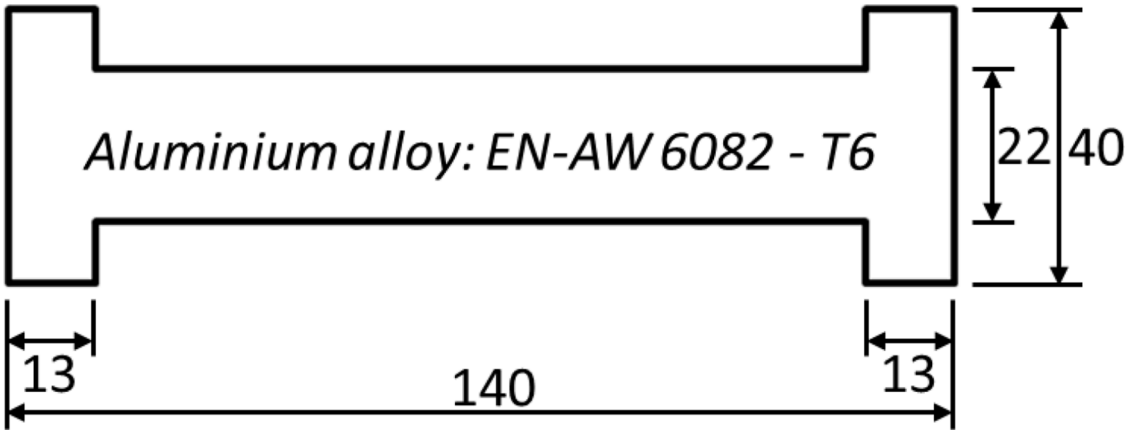

Fig. 8. Bridge girder cross-section (model scale; dimensions in mm).

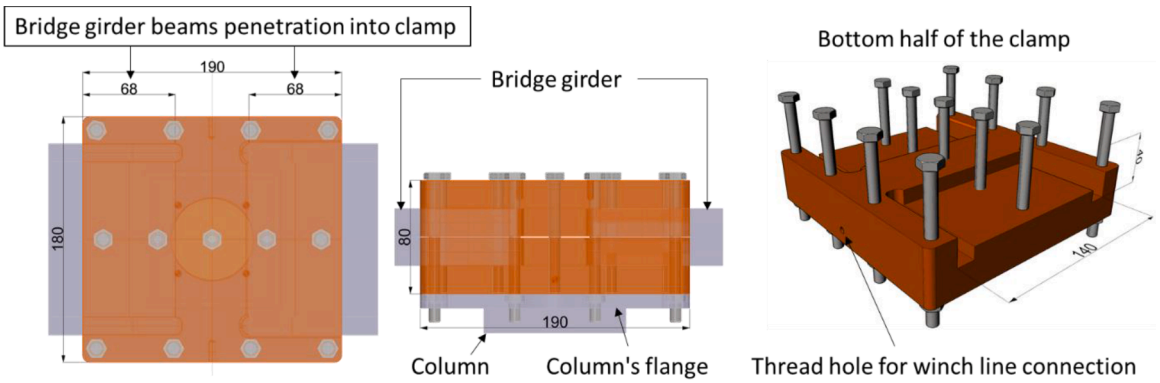

Fig. 9. Clamp geometry in model scale (units in mm); total mass of the clamp, bolts and nuts set is 6.471 kg.

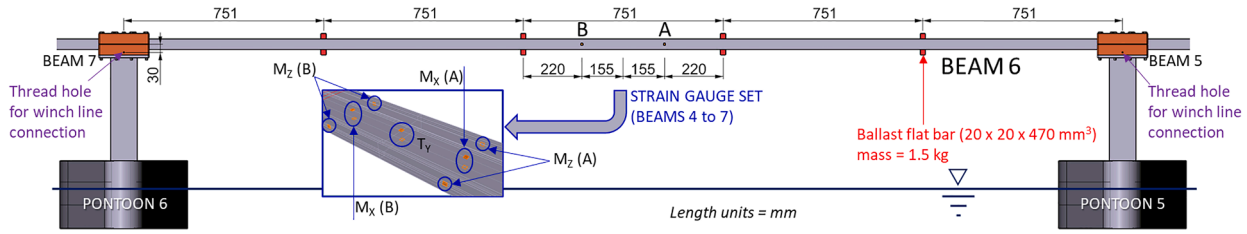

Fig. 10. Interior beams with ballast bars. Beams 4 to 7 are instrumented with strain gauge sets measuring (strong axis) horizontal bending moment at locations A and B (M_Z), (weak axis) vertical bending moment at locations A and B (M_X) and torsional shear between A and B (T_Y); shear force in way of A-B is obtained from the local differentiation of bending moment measurements. Dimensions in model scale.

this, a simply supported configuration for the entire bridge girder from pontoons no. 1 to no. 9 was considered for the bending stiffnesses, while a single span cantilever configuration was used for the torsional stiffness with the torque applied at the free end.

The bridge girder was manufactured by machining aluminium flat bar beams to the specified cross-sectional properties obtained from the cross-sectional uniformization procedure – see Table 6 for a list of properties and Fig. 8 for the cross-section geometry. Considering the generic bridge girder stiffness properties, an H profile was identified to be the most feasible geometry. Flat bar beams with 3700 mm x 40 mm x 140 mm (model scale) available in the market were used as raw profiles. The specified final cross-section was obtained by performing an optimization targeting the cross-sectional stiffness characteristics of the generic bridge girder. The H profiles were then machined out of the flat bars.

Each beam for the bridge girder's spans connecting pontoons no. 1 to no. 9 is 53 mm shorter than required for the target 125m span in full scale. An aluminium clamp type connection was designed to fasten the spans which could also accommodate for the missing 50 mm plus a 1.5mm construction clearance – see Fig. 9 for the geometry of the clamps and Fig. 10 for the assembly. The large number of bolts / nuts used in each clamp and the torque applied to them, was considered enough to avoid sliding of the beams for the bending moments at play which would otherwise induce damping due to friction during the tests.

At each extremity of the model, the bridge girder was extended beyond pontoons no. 1 and no. 9 so as to reduce the sagging static deflection that would otherwise be noticeable if the truncation would end at the pontoon locations. These extensions were made considerably rigid so that their flexural vibrations, especially in the vertical plane (weak axis), would not influence the results significantly. For this, brackets were welded bridging the columns to the extended girders – see Fig. 7. The longitudinal boundary condition applied at one of the extremities of the model is also represented in the same figure. Finally, ballast bars were fitted along the bridge spans and girder extensions to

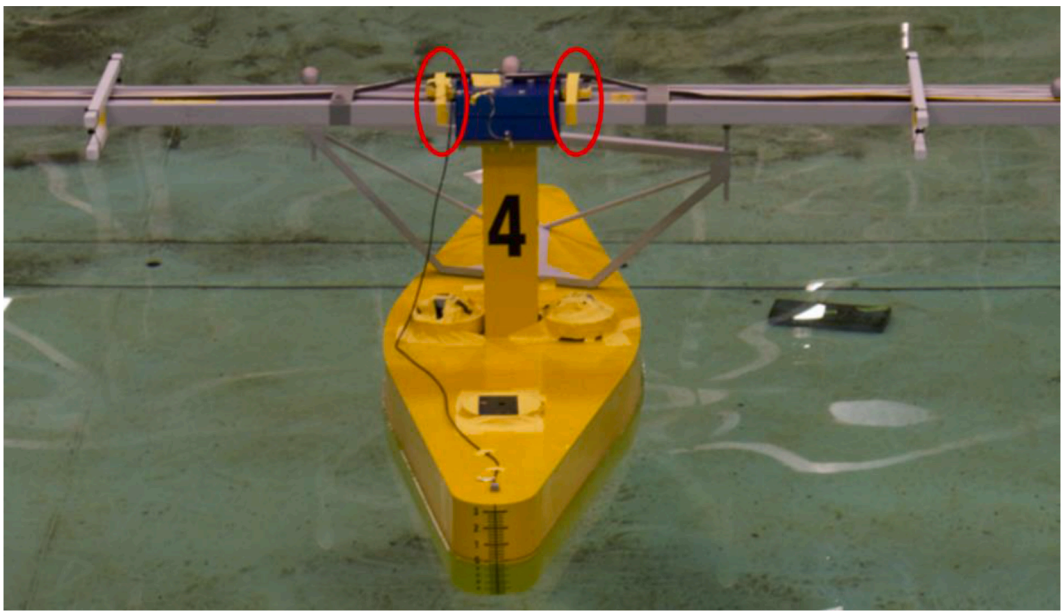

Fig. 11. Added ballast to compensate for inhomogeneity in the mass distribution of electrical wires along the bridge girder (number of wires reduces towards the centre of the model).

Table 7
Mooring system properties (full scale).

Line	Pontoon	Direction	Pre-tension		Spring set	Weight in water [kN]	Stiffness [kN/m]
			POS 1 [kN]	POS 2 [kN]	Pre-tension length (only spiral sections)		
F1	1	FWD	6 506	6 612	41.592	396.0	495.4
A1	1	AFT	6 423	6 593	40.626	386.4	495.4
F9	9	FWD	6 423	6 624	40.626	387.5	495.4
A9	9	AFT	6 468	6 692	40.793	387.9	495.4

NOTE: F[1;9] = towards wavemaker; A[1;9] = towards absorbing beach

Table 8
Bridge girder ballasting in full scale. "Diff" denotes difference to the generic bridge mass per length.

Pont	Half beam (towards free end of the model)					Half beam (towards constrained end of the model)				
	Ballast [tonne]	Cables [tonne]	Clamp*[tonne]	Total [kg/m]	Diff [%]	Ballast [tonne]	Cables [tonne]	Clamp* [tonne]	Total [kg/m]	Diff [%]
1	227.1	0.0	122.5	19 121	12.64	227.1	35.2	122.5	17127	0.89
2	227.1	18.0	140.3	17 136	0.95	227.1	17.2	140.3	17 124	0.88
3	227.1	16.5	141.4	17 130	0.91	227.1	11.7	141.4	17 054	0.46
4	227.1	7.2	151.6	17 146	1.01	227.1	6.4	151.6	17 133	0.93
5	227.1	2.6	152.6	17 087	0.66	227.1	8.1	152.6	17 176	1.19
6	227.1	10.0	145.7	17 097	0.72	227.1	10.8	145.7	17 109	0.79
7	227.1	15.3	139.5	17 081	0.63	227.1	20.1	139.5	17 158	1.08
8	227.1	20.8	131.0	17 032	0.34	227.1	21.6	131.0	17 044	0.41
9	227.1	22.3	122.5	16 919	-0.33	227.1	0.0	122.5	19 121	12.64

* Clamp mass includes additional ballast added in way of the Clamps No. 2 to 8 (see Fig. 11)

comply with the correct mass per unit length as shown in Figs. 7 and 10. An additional adjustment was carried out at clamp positions, corresponding to pontoons no. 2 through no. 8, by adding small ballast weights to account for the instrument related cabling non-uniform mass which ran along the bridge girder – see Fig. 11. The mass distribution along the bridge, present in terms of local segments surrounding each pontoon, is listed in Table 8.

The P85 pontoons were each fitted with a pair of transverse mooring lines, which were designed to comply with the boundary condition strategy described in Section 2.3.3 targeting the lateral restoring coefficients as determined using the numerical model – see Section 3.2. Each line is composed by (from the model anchor point to the bottom anchor point): swivel, force transducer, chain segment, 6 springs in parallel, chain segment, swivel. See Table 7 and Fig. 6 for a full description of the mooring lines.

3.2. Numerical model

A numerical model of the truncated design was modelled in SIMA/RIFLEX in full scale prior to the model tests in order to assess overall responses and check that the test runs would comply with the limitations of the experimental setup (e.g. maximum spring extensions in the mooring lines).

3.2.1. Bridge girder

The bridge girder runs along the y-axis, with y=0 at midway between the two P85 moored pontoons and the positive y direction from P1 to P9 – Fig. 12 shows an overall view of the numerical model's 3D

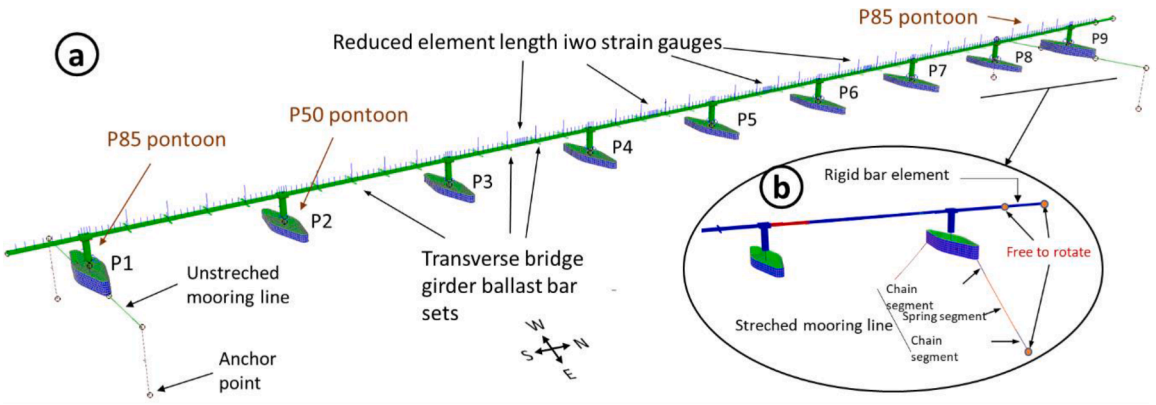

Fig. 12. Numerical model in SIMA/RIFLEX: (a) modelling view, (b) static condition.

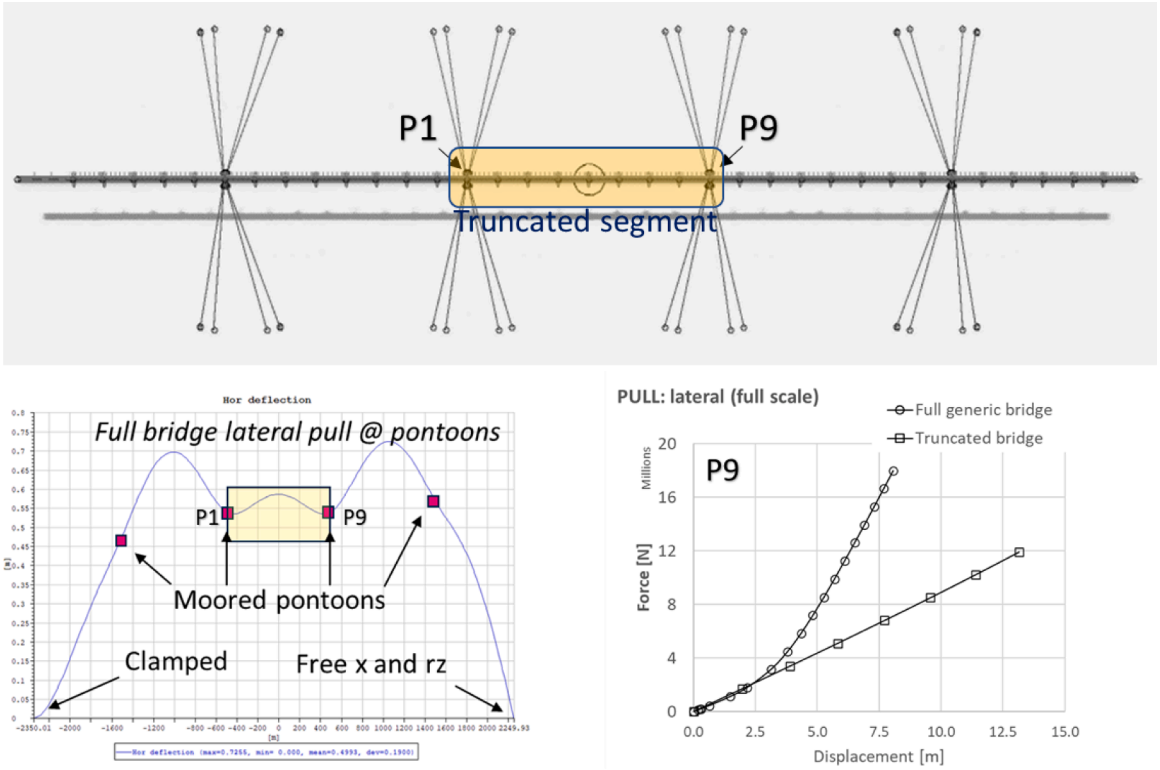

Fig. 13. Full scale lateral stiffness of truncated model at the (moored) P85 pontoons.

representation.

The cross section of the bridge is identical to the one in the physical model. The rigid transverse ballast bars and clamps are included as segments with correct additional mass corresponding to the physical model ones. Mind that the stiffness properties are kept the same as the girder, though. Numerical static loading tests carried out before the model tests, showed the difference in deflection of the bridge accounted to be less than 3% when considering the clamps as completely rigid (which they are not in reality), therefore the deviation arising from the continuous girder stiffness properties is considerably smaller than this relative to the real case.

3.2.2. Columns and pontoons

The columns are modelled by scaling the physical model columns properties to full scale. Pontoons are included as rigid floating bodies for which the individual wave frequency dependent hydrodynamic coefficients and second order mean drift quadratic transfer functions were obtained using WAMIT. Mind that hydrodynamic interaction between pontoons is not accounted for. The quadrant meshes used for these computations are shown in Fig. 4, where the double symmetry of the geometry is exploited for solving the potentials. The maximum edge length of each mesh element is 1.7m, which is known to provide good relevant outputs for drift force computations for wave periods higher than 1s when considering a 1/6 panel length required ratio to the incoming waves (DNV-GL 2017). Panels with a coherent reference length were used on the waterplane to remove the effect of irregular frequencies (not shown in the Figure).

The simulations in WAMIT comprised 130 frequencies, with a step of 0.04 rad/s, from 0.0 rad/s to 5.24 rad/s, in addition to the infinite frequency. From this data, RIFLEX computes the corresponding impulse response functions for the time domain hydro-elastic computations through the inverse discrete Fourier transform. Steady wave drift force coefficients are also computed by WAMIT and used in RIFLEX. The momentum formulation was used, so only the horizontal modes are

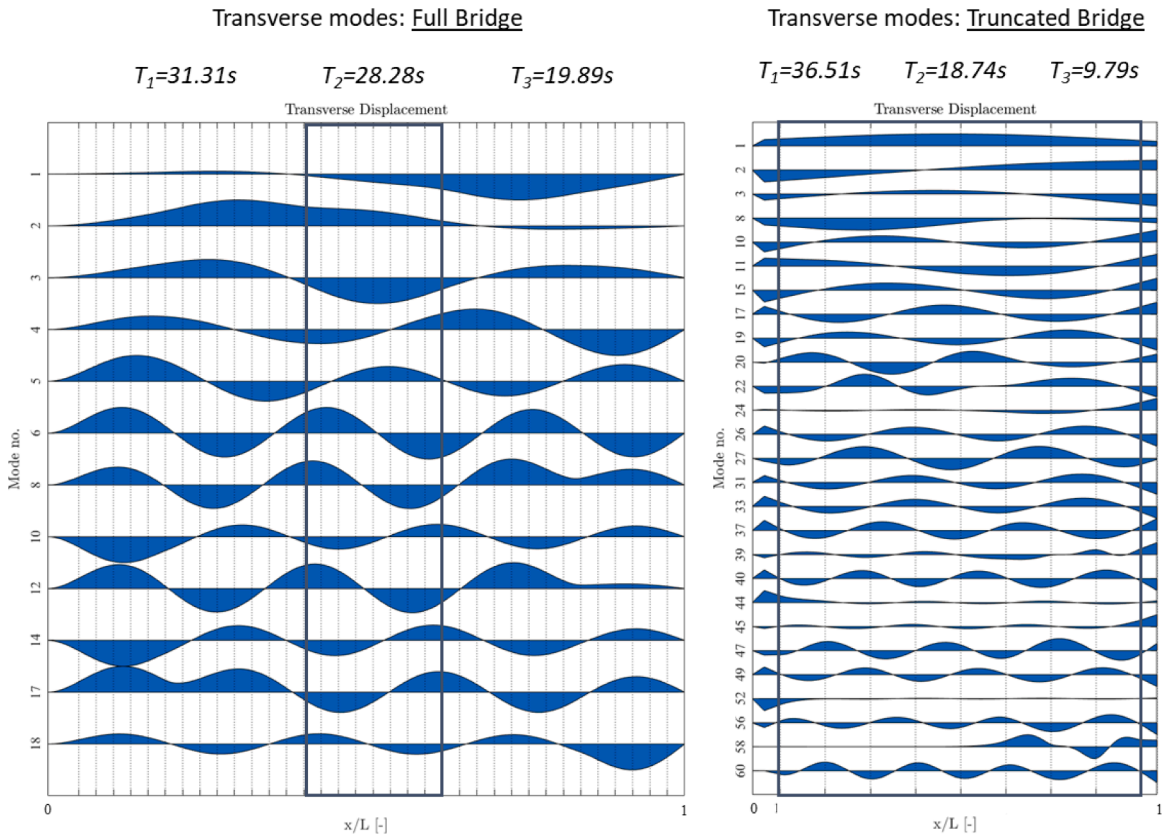

Fig. 14. First eigen vectors of the full generic bridge and truncated bridge with dominant lateral displacements. T_i corresponds to the eigen period for mode i of each configuration. Values in full scale.

considered.

3.2.3. Mooring

The longitudinal constrain at the end close to Pontoon 9 was made the same as in the physical model: a rigid bar with two ball connections at each end. The mooring is modelled as a segmented beam, for which the EA (E = young modulus, A= cross sectional area) corresponding to the spring stiffness was applied. No hydrodynamic effects were considered regarding the mooring lines.

In Fig. 13, the numerical lateral restoring curves for each of the moored pontoons is compared to that of the same pontoons on the full generic bridge. Here, one compares the position of the P85 pontoons in the truncated model with that of same pontoons in the full generic bridge. In both cases, a transverse horizontal force is applied to each pontoon (9 pontoons in the truncation and 35 pontoons in the full bridge). It is clear from Fig. 13 that the full bridge restoring curve is only linear up to 3 m displacement, from which point the remaining structure of the bridge, including the land connection boundary conditions and additional mooring clusters, start to have an added effect to the local mooring stiffness. The restoring non-linearity could be accounted for by usage of multiple stepped actuating springs, but in the current study one opted to simplify and use a linear system. The exact lateral stiffness to target was then chosen as the one corresponding to the mean drift, without wind, for the 100 years limit sea state ("DC 3" in Table 4) computed using the numerical model of the generic bridge described in Section 2.1: 706 kN/m. This was considered a reasonable overall approach considering the tests to be carried out in the experimental campaign. It is worth mentioning that each mooring cluster lateral stiffness in the reference bridge (Section 2.1) for small displacements is 1.5 MN/m. Then the truncated version should be roughly half of that, for there are only two moored pontoons in contrast to four and no land connections, which is in line with the calculated results.

3.2.4. Eigenmodes

The numerical model was also used for estimating the physical models' flexural eigen-modes – see Figs. 14 and 15. The modes of the full length reference bridge numerical model do not match those of the truncated model used in the experiments, although some correlation exists especially for the modes with predominantly vertical displacement. Both results were computed with SIMA, and it is worth making notice that SIMA uses the zero-frequency added mass to compute the eigenmodes, irrespective of the natural frequency of each, which may lead to small but not negligible inaccuracies.

4. Experimental setup and selected test matrix

4.1. Position of the model, wave and current generation

The basin floor was set to 1.5m depth (49.95 m in full scale) in accordance with the truncation strategy in Section 2.3. The basin is fitted with two sets of wavemakers (Fig. 5). Along the 50 m side there is a continuous double flap (denoted BM2) hydraulically operated unit for generating long-crested, regular and irregular waves. The second wavemaker, fitted along the 80 m side of the basin (denoted BM3), consists of altogether 144 individually controlled flaps. This unit can generate short-crested seas within a wide range of directional distributions of the energy. The current generating system of the basin is based on pumping water around the adjustable floor.

The model was positioned in two configurations in the basin: positions A and B in Fig. 16. Position A was used for tests with combinations of regular and irregular long crested waves, current and wind – all acting perpendicular to the bridge longitudinal axis. Position B was used for tests with an inhomogeneous irregular wave and regular and irregular oblique waves.

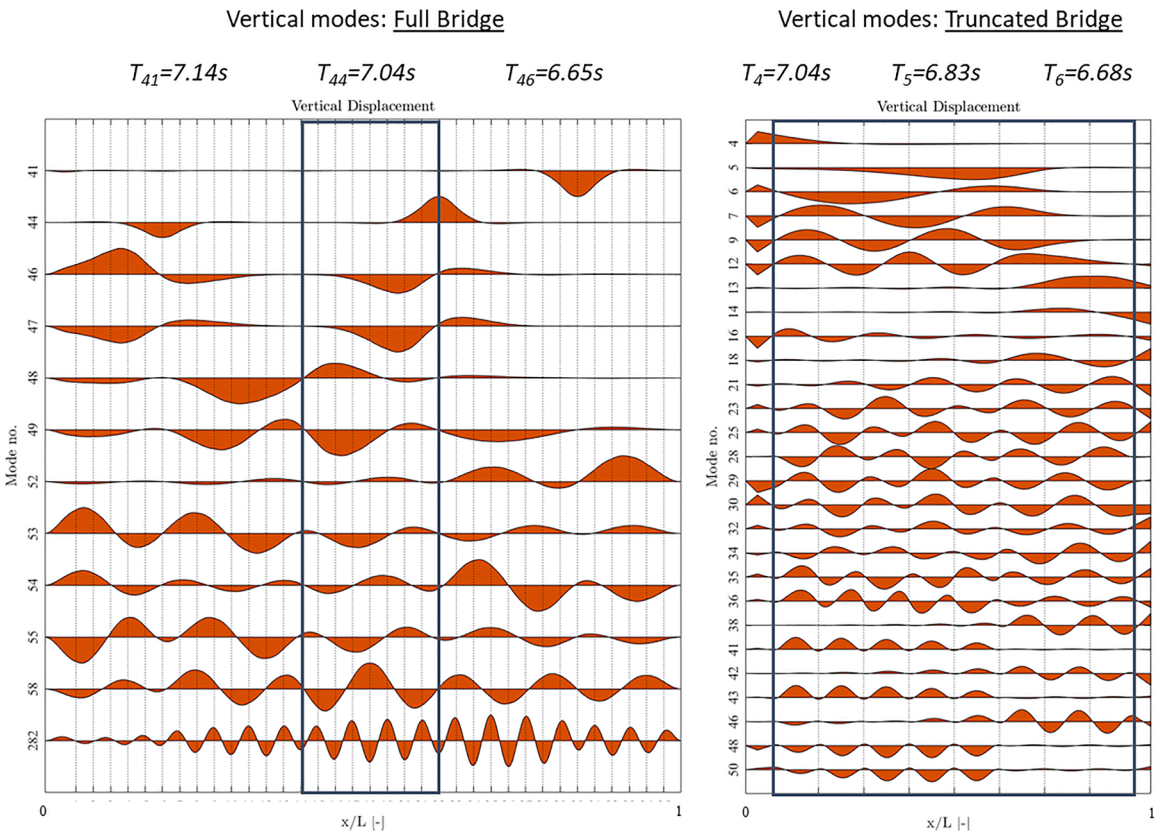

Fig. 15. First eigen vectors of the full generic bridge and truncated bridge with dominant vertical displacements. T_i corresponds to the eigen period for mode i of each configuration. Values in full scale.

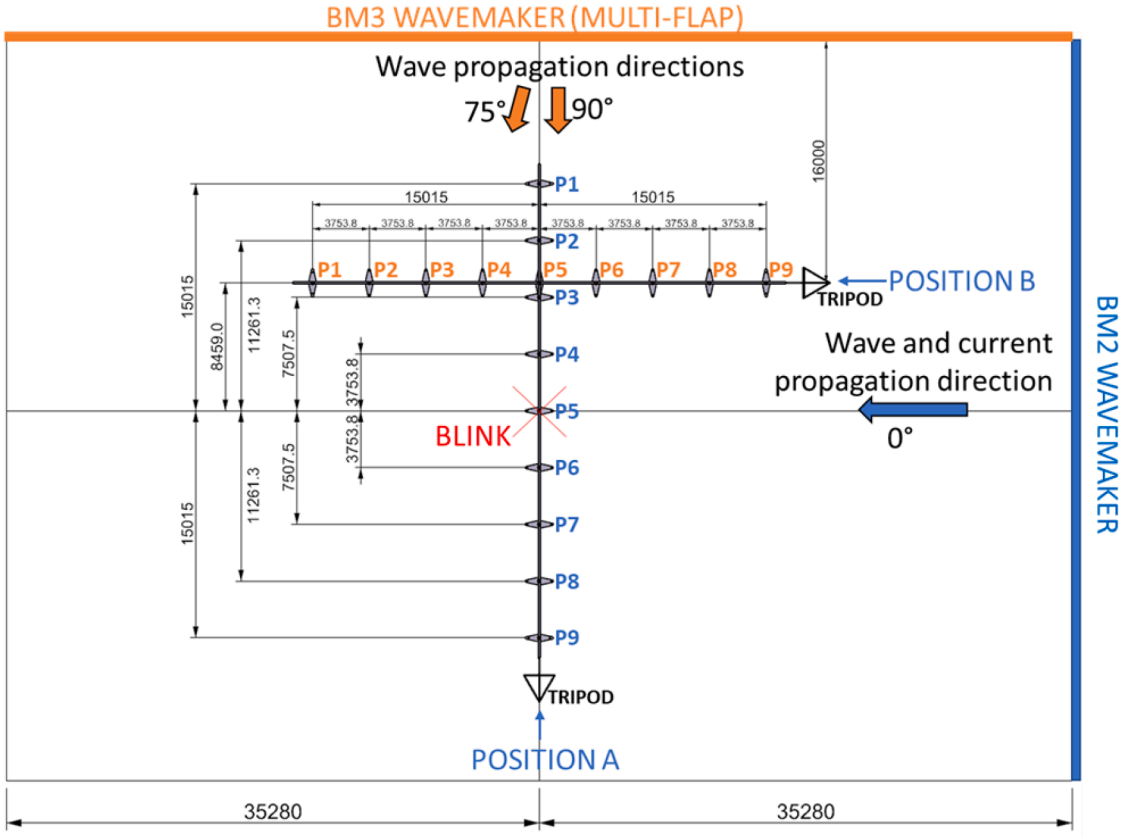

Fig. 16. Positions of the model in the basin (model scale, dimensions in mm). "BLINK" denotes the centre of the basin.

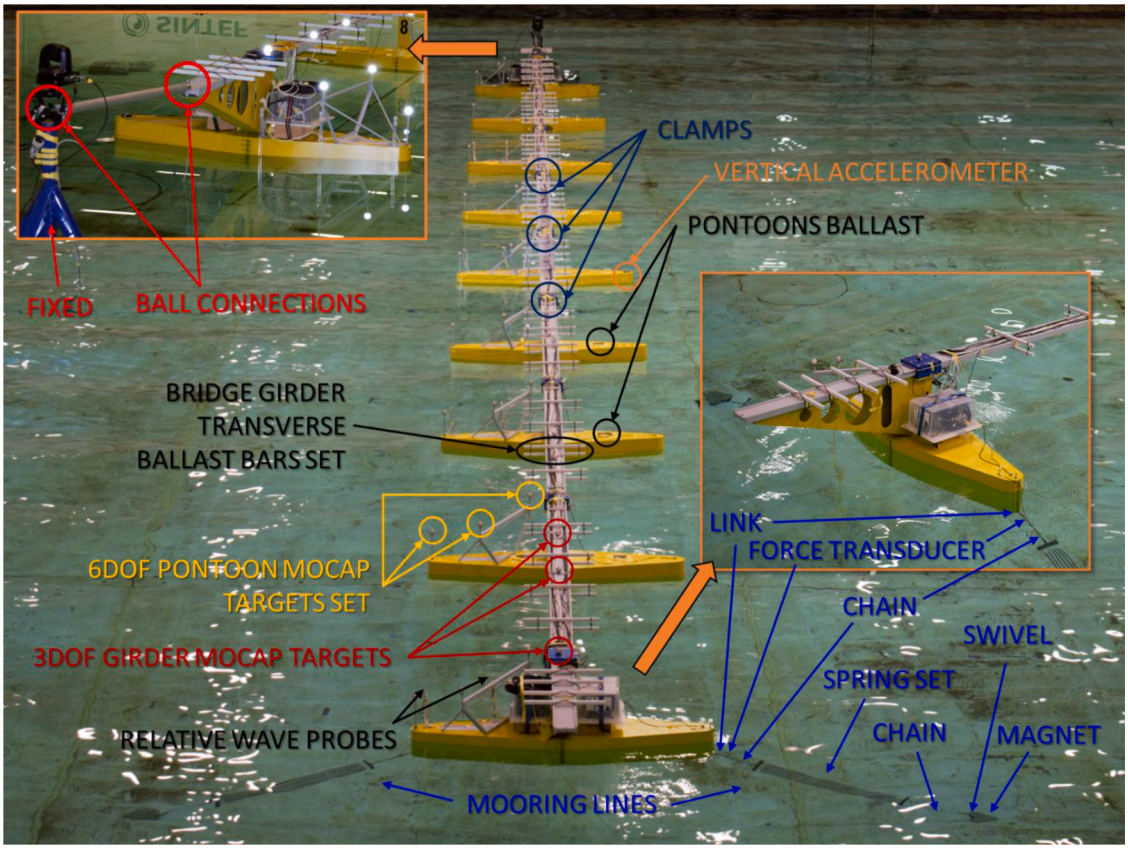

Fig. 17. Instrumentation in the model.

4.2. Generation of wind forces

The action of the wind was emulated by connecting the bridge girder at the intersection of each pontoon to a set of nine actuator winches through a thin wire. At each of these locations, a lateral dynamic force is applied following a prescribed time series acting solely in the same direction of the wave, or current propagation, or towards the beach opposing the wavemaker BM2, depending on the test specific load condition. The time series varies between locations and was obtained from numerical simulations (not described here) for prescribed wind spectra conditions along the bridge using the numerical model of the generic bridge described in Section 2.1. The forces applied are then the result of discretising these forces into the aforementioned longitudinal locations of the truncated model, i.e. at each location the mean plus turbulent force is the total force acting between the mid span to the left and the mid span to the right of each pontoon. The wind conditions initially targeted were the ones corresponding to DC 1 and DC 3 in Table 4. However, the numerical predicted mean forces together with the current and wave actions for higher sea states resulted in considerable lateral motion extremes in the preliminary verifications with numerical model, therefore requiring a more complicated mooring spring arrangement to cover only a small sub-set of environmental load conditions. As the intensity of the wind was not paramount for the objectives of this study, the wind forces were reduced to 25% of their value to ensure that the mooring springs would not be damaged. This approach was later found to be overly conservative.

4.3. Measurements and instrumentation

The instrumentation used during the tests comprised the following measurements:

- Vertical acceleration at a point in each pontoon, plus 3DOF acceleration at Pontoon no. 5 and corresponding clamp using accelerometers.
- Bending moments and shear forces in the four interior beams using strain gauges (see Fig. 10).
- 6DOF motions of each pontoon using a motion capture system (MOCAP) where a unique set of 3 rigidly connected targets is fitted on each pontoon.
- 3DOF motions at several points distributed along the bridge iwo of the bridge girder upper face, using single targets for the MOCAP.
- Tension forces at each mooring line and each winch line using axial force transducers iwo of the corresponding "fairlead" points.
- Relative wave elevations at every other pontoon using wave probes connected to the pontoons' deck.
- 3DOF force measurements at the connection to the bottom fixed tripod using a tri-axial force transducer.
- Wave elevation at 5.0 m (in model scale) in front of Pontoons P1, P5, and P9 (direction towards the wavemaker) using bottom fixed wave probes.
- Wave elevations at the centre of each pontoon for both positions of the model during environment calibration using bottom fixed wave probes.
- Wave elevations with a 15-wave probe double circular array distributed for relevant positions of the pontoons during the environment calibration phase (see Section 5.1).
- Current measurements at the position of pontoon no. 5 during wave current calibration and at another position during tests with the model placed using a current sensor.

A view of the model with the identification of the main instrument components is shown in Fig. 17.

Table 9
Full scale selected environmental conditions from the experimental campaign. H_S and T_P denote significant wave height and wave peak period, respectively. H and T denote wave height and period for the case of tests with regular waves. Values in full scale.

Test ID	Wave type	Test type	H or H_S [m]	T or T_P [s]	Current [m/s]	Wind [Return period, years]
2010	-	Current	0.0	0.0	1.0	-
2020	-	Current	0.0	0.0	1.4	-
2111	-	Wind	0.0	0.0	0.0	1
2120	-	Wind	0.0	0.0	0.0	100
2133	Irregular	Wind + Current	0.0	0.0	1.0	1
2140	Irregular	Wind + Current	0.0	0.0	1.4	100
2510	Irregular	Broadband	1.0	N/A	0.0	-
2611	Irregular	Waves	1.6	5.3	0.0	-
2630	Irregular	Waves	1.3	7.1	0.0	-
2710	Irregular	Waves + Current	1.6	5.3	1.0	-
2730	Irregular	Waves + Current	1.3	7.1	1.4	-
2810	Irregular	Waves + Wind	1.6	5.3	0.0	1
2830	Irregular	Waves + Wind	1.3	7.1	0.0	100
2910	Irregular	Waves + Current + Wind	1.6	5.3	1.0	1
2930	Irregular	Waves + Current + Wind	1.3	7.1	1.4	100
3230	Irregular	Waves (inhomogeneous)	1.4	6.6	0.0	-
2211	Regular	Waves	0.66	6.25	0.0	-
2220	Regular	Waves	1.32	7.00	0.0	-
2230	Regular	Waves	2.00	12.50	0.0	-
2241	Regular	Waves	1.00	6.25	0.0	-
2250	Regular	Waves	2.00	7.00	0.0	-
2260	Regular	Waves	3.00	12.50	0.0	-
2310	Regular	Waves + Current	0.66	6.25	1.0	-
2320	Regular	Waves + Current	1.32	7.00	1.0	-
2330	Regular	Waves + Current	2.00	12.50	1.0	-
2340	Regular	Waves + Current	1.00	6.25	1.0	-
2350	Regular	Waves + Current	2.00	7.00	1.0	-
2360	Regular	Waves + Current	3.00	12.50	1.0	-
2411	Regular	Waves + Current	0.66	6.25	1.4	-
2420	Regular	Waves + Current	1.32	7.00	1.4	-
2430	Regular	Waves + Current	2.00	12.50	1.4	-
2440	Regular	Waves + Current	1.00	6.25	1.4	-
2450	Regular	Waves + Current	2.00	7.00	1.4	-
2460	Regular	Waves + Current	3.00	12.50	1.4	-

4.4. Selected environmental load test matrix

The environmental conditions in Table 4 correspond to JONSWAP spectra with a significant spreading and a very reduced peak enhancement factor, which were challenging to be modelled in the ocean basin such that the full model would be covered. Therefore, only long crested seas were modelled and these with reduction factors of H_S relative to the values in Table 4 for the wave headings perpendicular to the bridge girder. Failing to do so would result in unrealistic and dangerous motions of the model as, contrary to the real environmental design conditions, all the wave energy is concentrated in one heading that excites all the pontoons with the same phase.

A total of 96 tests with current and/or waves without the model present for undisturbed incoming wave identification, 6 static deflection tests and 12 pull-out and decay test for system identification, and 56 tests with combinations of current, wind and waves with the model present, were carried out. The full test matrix included tests with regular and irregular waves with varying periods and heights, with different combinations of wave and current. Tests with oblique regular and irregular waves (without current) were also carried out. Swell components were not modelled. A selection of these tests is included in the present paper and shared publicly, which the authors believe to be a meaningful set (see Table 9 for a list of the load conditions). The set corresponds to:

- 3 h tests with concurrent wind, current, and long crested irregular waves, in addition to the tests with each of these environmental components isolated.
- A 1 h realization of a broad spectrum long crested seasate test, and tests in regular waves with different combinations of current, from which response amplitude operators can be identified.
- A 3 h test amplitude-wise long crested inhomogeneous sea state.

4.5. System identification tests

In addition to the tests with environmental load conditions, system identification tests were carried out. These included: (a) static vertical deflection and torsion twisting tests, by deploying weights at selected locations at selected pontoons; (b) pull out tests at the end pontoons for assessing the lateral mooring stiffness; (c) distributed pull out tests with nonuniform forces applied along the bridge deck in way of each pontoon; (d) decay tests following the release of the model from the pull outs described in the previous two points. Mind that the actuator winches were used for the distributed pull out and decay tests. This solution not only made the distributed loading tests practicable, but also allowed for a high precision prescribed force to be easily applied.

5. Undisturbed waves and current

5.1. Environment calibration and documentation

The irregular waves were calibrated using the measured wave elevation at the centre of pontoon no. 5 as a reference for each of the A and B positions of the model. From the prescribed spectral properties, an optimal numerical realization of the wave spectrum which better approximates these parameters was chosen and then iterated experimentally. Mind that random phases and amplitudes were used to generate the realizations, as it has been shown that only these can truly represent a Gaussian sea statistical property, e.g. in terms of wave group statistics (Tucker et al., 1984). An example of the procedure is shown in Fig. 18, where the target theoretical spectrum, the numerical realization, and the measured spectrum are shown. The broadband, regular, and inhomogeneous, waves were not experimentally iterated, for the objectives towards exploitation of these load conditions do not require a very precise prescribed wave heigh and period experimental realization.

While the waves were calibrated at the aforementioned reference positions, the wave elevations were identified at all positions of the pontoons in both configurations, either with a single wave probe or with the circular wave probe array. A 2-phase procedure was implemented in practice to limit the number of wave probes in usage at the same time and make the process more efficient timewise. See Fig. 19 and Fig. 20 for the global positions of the probes, and Fig. 21 for the geometry of the wave probe ring. The circular wave probe array was deployed in the regions close to the beach opposite to the BM3 wave maker in configuration A, as refraction effects were predicted to be higher in those regions with waves generated by BM3 wave maker. For configuration B, the circular wave probe array was deployed in the first two pontoon positions closer to BM2, for the case of oblique waves generated by BM3, as wave lateral energy dissipation in the direction towards BM2 at those locations could be non-negligible. Finally, the circular wave probe array was deployed at all of the pontoons' positions in configuration A for the case of the inhomogeneous seastate generated by BM3 – see Section 5.2.

In Fig. 22 a segment of the time series of the free surface elevation at several pontoon positions is shown for one of the tests. It is clear that perfect homogeneity is not achieved as there are local distortions on the wave crests arising from parasitic phenomena on the ocean basin which are magnified by the extreme ratio of the identification zone's length by the wave significant height: 625! On the other hand, the corresponding spectrum based estimated statistical properties show a clear coherence with very limited variations of H_S and T_P in Table 10.

The current was calibrated following an iterative procedure of

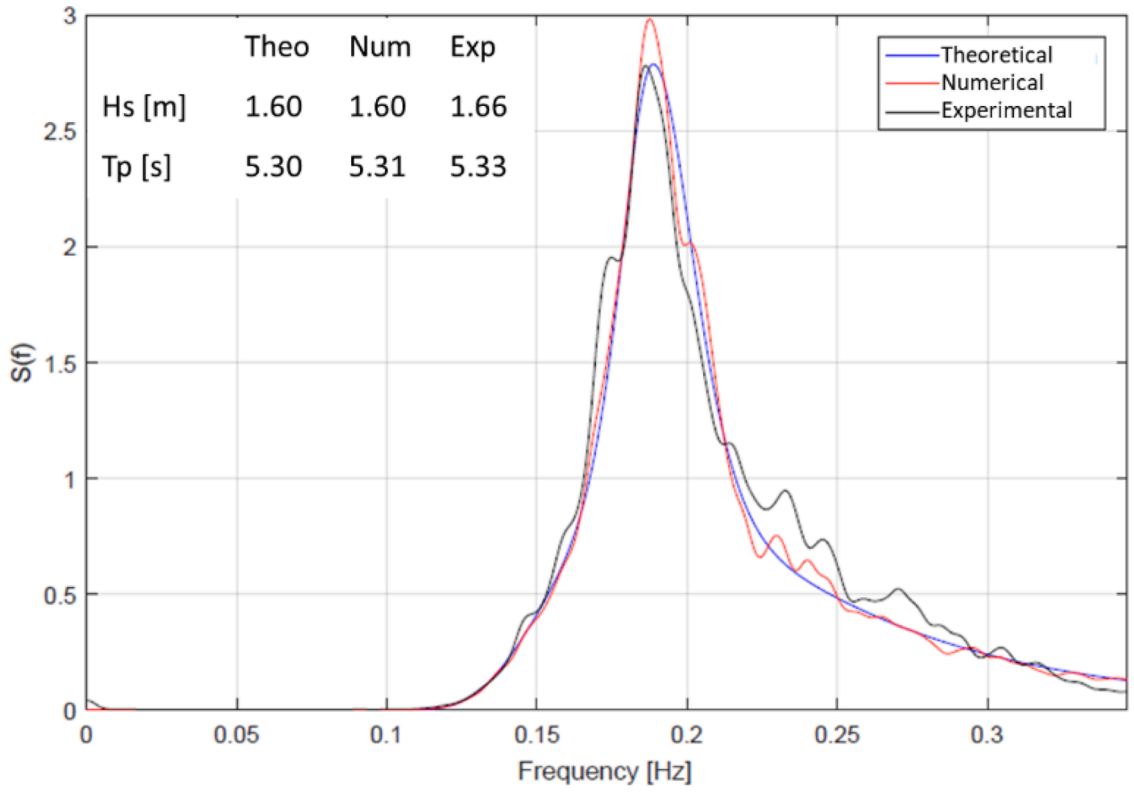

Fig. 18. Full scale wave spectrum calibration at the centre of pontoon 5 (model position A) for environmental conditions in tests 2611 and 2810 in Table 9.

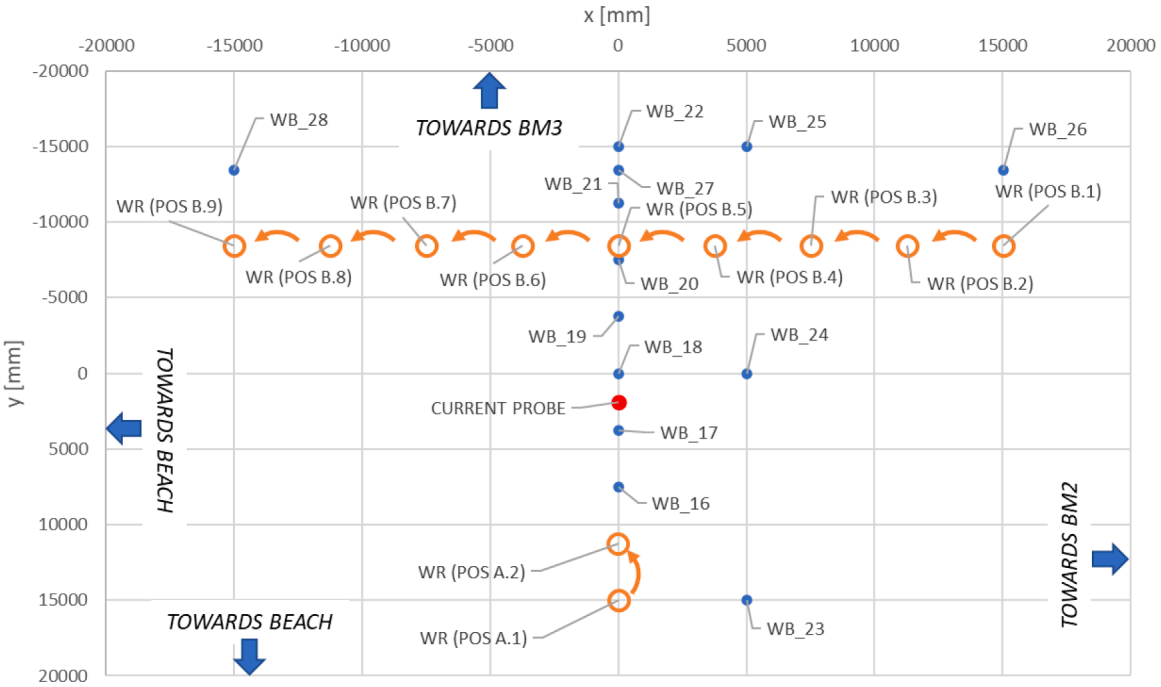

Fig. 19. Wave probes and current probes positions for Phase 1 environment calibration and documentation (model scale). Circles denote deployment of wave probe circular array with arrows representing the modification of the array position upon repetition of generated waves; blue dots represent single wave probes. Probe sets (WB_28,WB_27,WB_26) and (WB_23,WB_24,WB_25) are placed 5m (in model scale) ahead of the model for model positions A and B, respectively.

adjusting the current generating pumps power until the reasonable values were achieved regarding mean values and standard deviations – see Table 11. The Current was measured at a depth of 2.5m, in the same horizontal position of the centre of pontoon no. 5, corresponding to half the draft of the P50 pontoons.

5.2. Inhomogeneous sea state

The inhomogeneous sea state was generated by linearly varying the amplitude of the flap motion in the multi-flap wavemaker BM3 from 100% to 50% along the length of the wavemaker as depicted in Fig. 23.

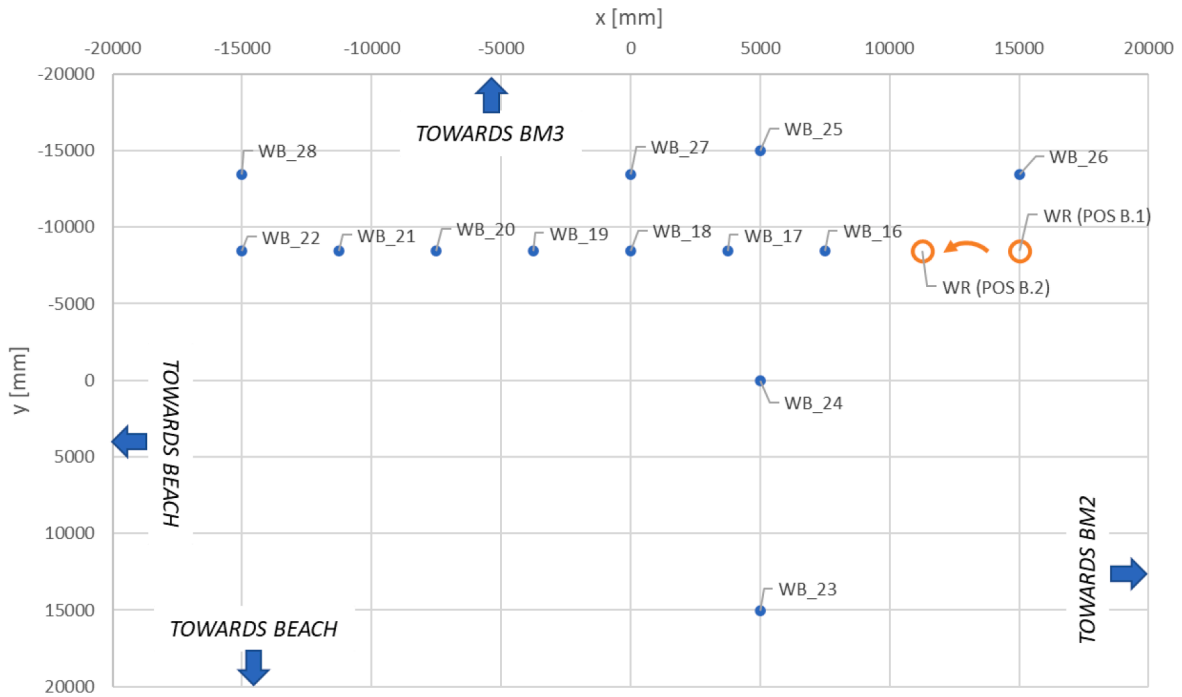

Fig. 20. Wave probes and current probes positions for Phase 2 environment calibration and documentation (model scale). Circles denote deployment of wave probe circular array with arrows representing the modification of the array position upon repetition of generated waves; blue dots represent single wave probes. Probe sets (WB_28,WB_27,WB_26) and (WB_23,WB_24,WB_25) are placed 5m (in model scale) ahead of the model for model positions A and B, respectively.

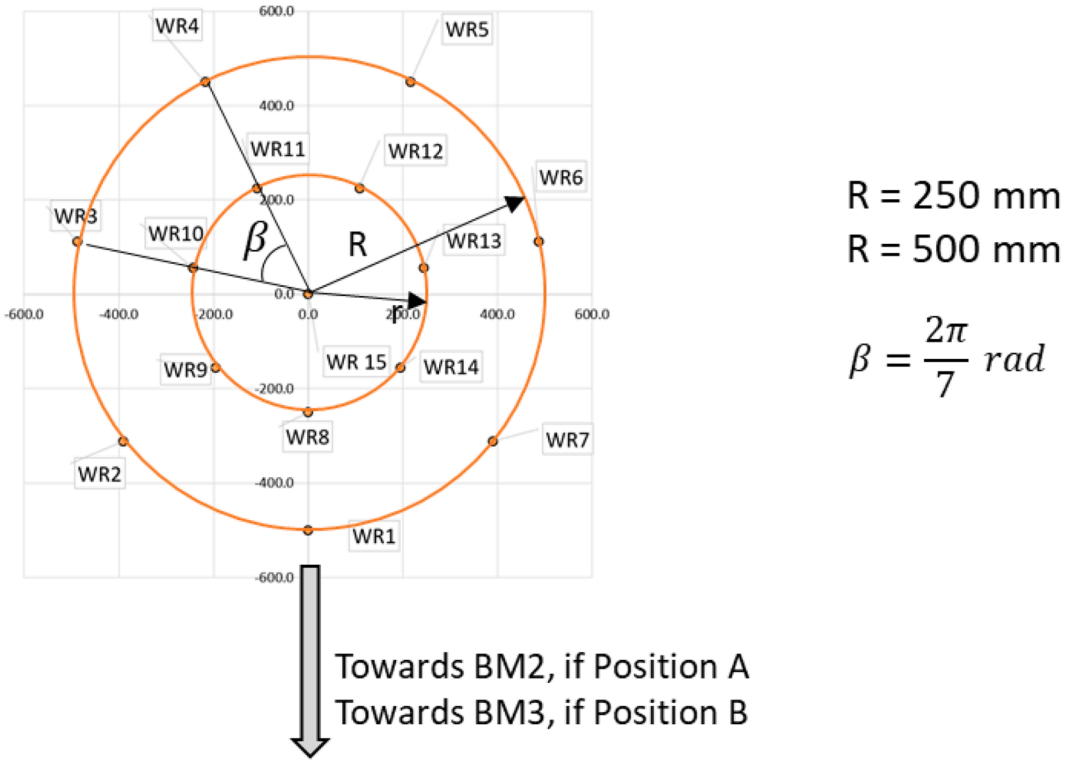

Fig. 21. Wave probe circular array (denoted "WR" in Figs. 19 and 20). Dimensions in mm (model scale).

For this sea state, the circular wave probe array was deployed in each position corresponding to the centres of the pontoons in order to have a very good documentation of the undisturbed wave. Fig. 24 shows the estimation of the two-dimensional spectra using the maximum entropy method (Nwogu, 1989) for the first, middle, and last, pontoons resorting to the wave elevation data from the wave probe array at each of these locations. Fig. 25 presents the one-dimension spectra at every other pontoon for the same sea state. From these two figures, the spectra are seen to be those of long-crested seas with direction perpendicular to the bridge and with a very close to linear variation of significant wave height along the bridge.

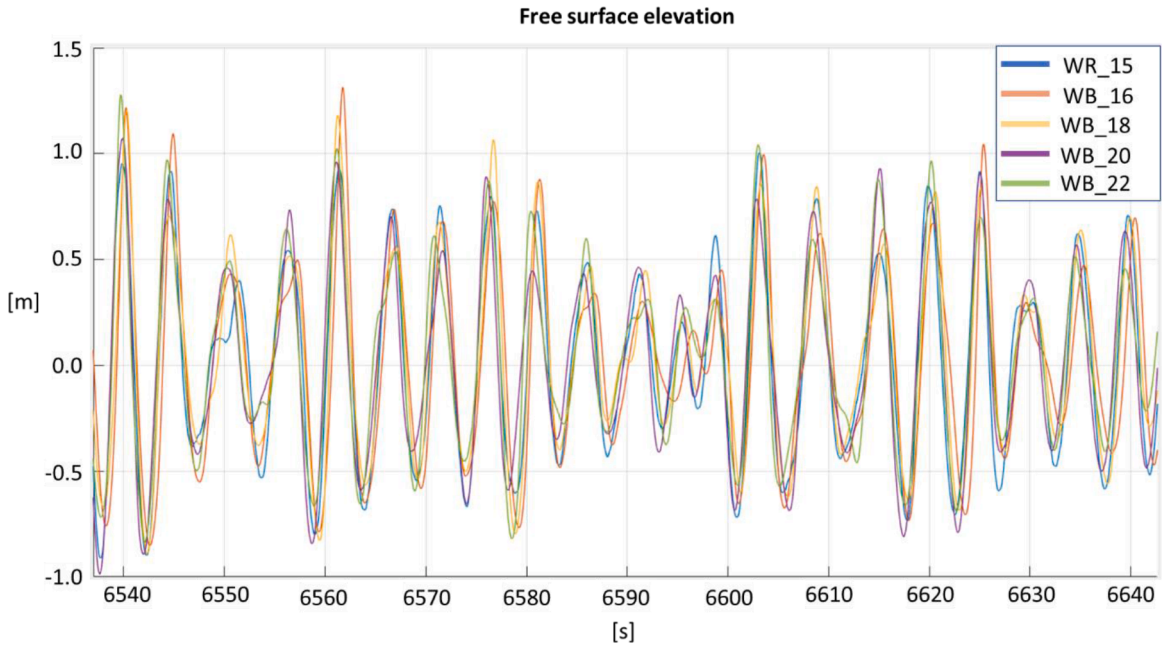

Fig. 22. Full scale free surface elevation at five positions along the model during calibration of wave conditions for tests 2611 and 2810 in Table 9; see Fig. 19 for location of wave probes.

Table 10
Spectral based estimations of full scale free surface elevation properties at five positions along the model during calibration of wave conditions for tests 2611 and 2810 in Table 9. See Fig. 19 for location of wave probes.

Position	Hs	Tp [s]
P1	1.562	5.37
P3	1.607	5.35
P5	1.625	5.39
P7	1.599	5.37
P9	1.651	5.36

6. Selected results and model verification and calibration

Raw model test data for the chosen dataset corresponding to the load conditions in Table 9 are available and fully described at Mendeley Data (Rodrigues, 2022). It includes the motion responses of the pontoons, forces at the mooring lines, among other.

This section presents results that are important for assessing the exploitability of the model test campaign and not of outputs relating to the exploitation of the campaign itself. This important distinction is underpinned by the objective of this paper, which is focused on how the model tests were designed, planned and carried out while at the same time sharing some of its results for being prospectively used as a benchmark by researchers in their numerical models' validations.

A selection of validation and calibration actions of the numerical model described in Section 3.2, from the results of what are commonly denoted documentation tests, is presented. Comparisons of selected calibrated numerical and experimental response amplitude operators and of the responses for one of the irregular waves' conditions are also given.

Note: In several of the plots, reference is made to (XPOS, YPOS, ZPOS), which denote translational positions of each pontoon in the earth fixed system with the same orientation as that shown in Fig. 2 – corresponding to (X,Y,Z)– but with origin at the centre of the waterplane of each pontoon,. Likewise, "Roll", "Pitch" and "yaw" correspond to angular motions' Euler angles of each pontoon using the sequence Yaw-Roll-Pitch.

Table 11
Current calibration (full scale).

Target current	Measured mean deviation	Measured standard deviation relative to the mean
1.0 m/s	+1.22 %	5.61 %
1.4 m/s	+0.57 %	4.84 %

6.1. Static loading

The objective of the static load tests was to verify the correct modelling of the structural elements in the scaled model from a static response perspective focusing on the bridge girder. Although all beams composing the bridge girder had been individually tested on a dry bench to calibrate the strain gauges and verify the response of each beam to known loads, only with the model fully assembled was it possible to perform validation (or calibration) of structural parameters that are relevant for the exploitation. An example is to establish the stiffness properties of the bridge girder beams to be used in a numerical model with the approach described in Section 3.2.1 for the modelling of the cross-sectional inertia parameters within the sections with the clamps connecting the bridge girder with the columns arising from each pontoon.

In order to isolate the response of the model from the mooring, and also allow for a shallow water configuration which made these tests much easier to carry out, the model was put in a free-floating position at a reduced bottom depth. Ballast weights were added in pontoons no. 1 and no. 9 to compensate the lack of the mooring pre-tension. Likewise, a weight was added to one of the end beams at the pinned connection with the pipe connecting the model to the tripod support (see Fig. 7) to compensate for the lack of the connection.

Six static loading tests were carried out covering various combinations of mass weights distributed on top of different pontoons' "decks". A torsion verification is shown in Fig. 26, namely on measured torque at the midspan of the four interior beams and trim of the pontoons. The numerical results presented in the figure include a 0.9 correction factor applied to the modelled torsional stiffness. Here it is important to realise that the formulation for torsional stiffness used was only approximate; specifically, case 6 of Table 10.2 in Young et al. (2012) was used. A verification of vertical deflection of the pontoons and measured bending moment at the four interior beams imposed by hoisting pontoon no. 5 is

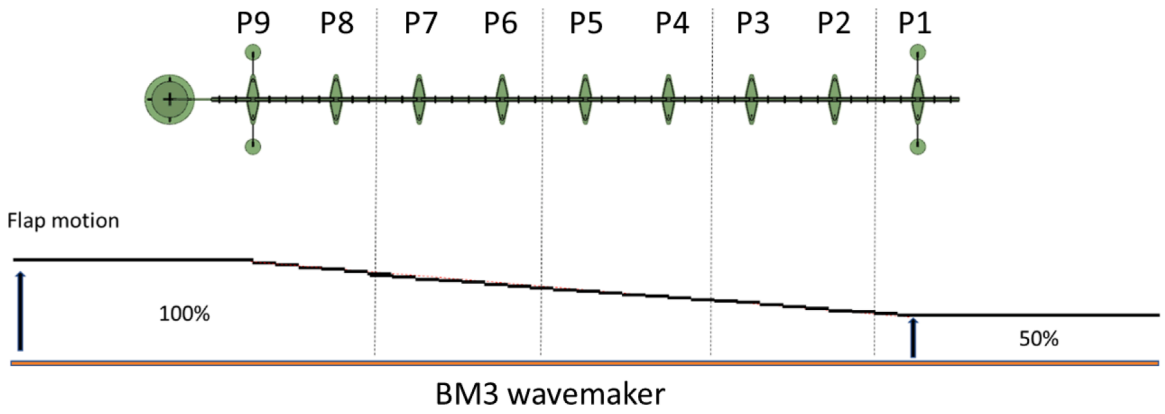

Fig. 23. Generation of inhomogeneous seat state (test 3230 in Table 9): flap motion relative stroke.

presented in Fig. 27. Here, the experimental measurements agree remarkably well with the numerical predictions, with deviations never exceeding 2%. In both bending and torsion cases, uncertainties related to the beams' Young modulus and shear modulus may also be additional causes of deviations.

6.2. Lateral pull-outs

A set of horizontal pull-out and decay tests with the initial forces (in model scale) as shown in Fig. 28 was carried out, therein denoted "PD" for "Pull-out and Decay". The actuator winches were used to pull the model at each clamp. This allowed for a very slow and controlled execution, making way for a practically continuous quasistatic assessment of the measured quantities from 1 N applied at each clamp to the final (before release) force distributions shown in Fig. 28. Comparison of the horizontal static response of test "PD5" between the experiments and the numerical model for the same static force distribution is shown in Fig. 29 for the lateral position of the pontoons, the horizontal bending moment, and the tension at the mooring lines – all relative to the initial unloaded condition. Here, results show an excellent coherence along the bridge. Analysis of the pull outs curves and the ones generated in Section 6.1 give a very high confidence regarding the properties of the physical model in terms of parameters that affect quasi-static responses.

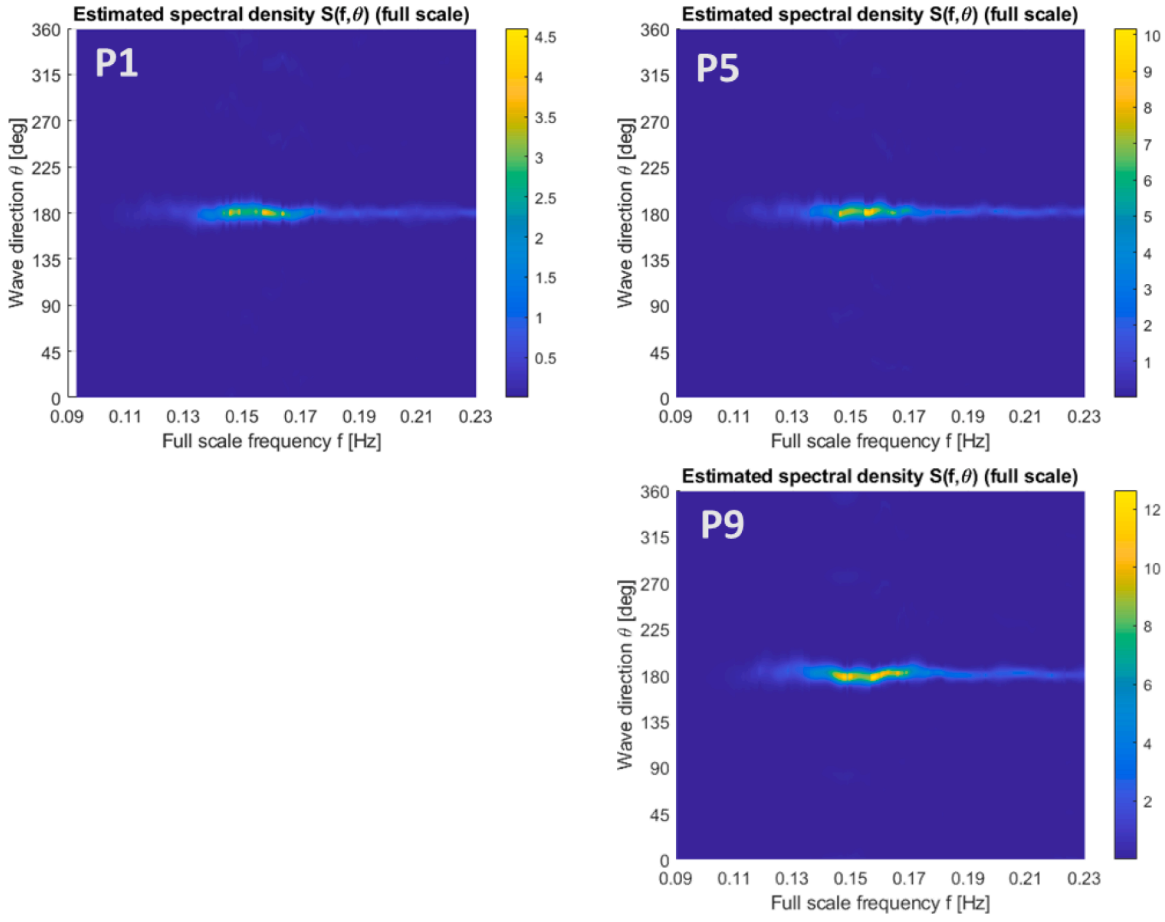

Fig. 24. Estimated two-dimensional full scale undisturbed wave spectral density across the model for test 3230 in Table 9.

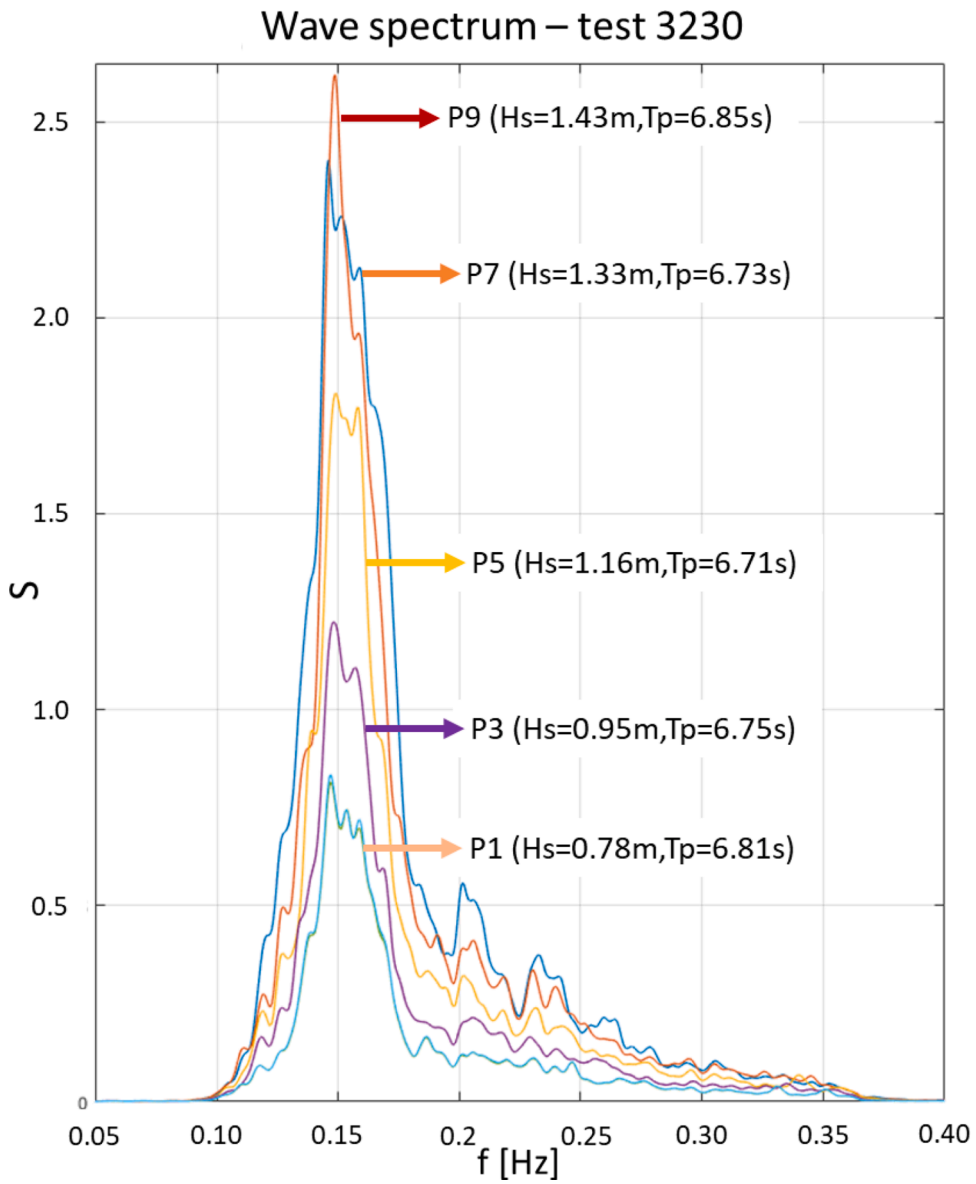

Fig. 25. Estimated one-dimensional full scale undisturbed wave spectral density across the model for test 3230 in Table 9.

6.3. Lateral decays

Decay tests were carried out by releasing the model from the initial conditions shown in Fig. 28. This was done by suddenly setting the actuator winches into *following mode*, i.e., following the free damped oscillations so that the effect of the force exerted by the actuators was virtually zero.

Responses of three decay tests are shown in Figs. 30–32. In particular, comparisons are made between the experiments and the numerical model (where quadratic and linear damping coefficients have been calibrated with the empirical results) for mooring line tensions, lateral motion of the pontoon P5, pitch motion of pontoons P1 and P5, and the strong axis bending moment at the mid spans of beams no. 4 and 5 – see Figs. 10 and 12 for beam number identification. Observation of these plots reveals that the starting quantities compare remarkably well, and the dynamic response is also in very good agreement, both concerning the time series and the spectral plots for period identification. This good correlation includes the appearance of a relatively strong secondary peak for the mooring tensions and lateral position of P5 for decay response to initial condition PD3 (Fig. 31), which is very well reproduced in the numerical simulation; and the high frequencies present in the initial instants of pitch decay, also reproduced to some extent in the three tests.

6.4. Response amplitude operators

Experimental to numerical response amplitude operators (RAO) comparisons for the motions are shown in Fig. 33. In this figure, estimates of the RAO are made using the broadband wave load condition 2510 in Table 9 for the experimental output. Regarding the numerical outputs, two types of simulations have been done: one with the input wave elevation on all pontoons as given from the experimental undisturbed wave elevation measured at the position of Pontoon no. 5, and another where individual regular wave load conditions covering the frequency range of interest was simulated. It is important to stress that in the numerical simulations the hydrodynamic multibody interaction is not accounted for.

Analysing the results in Fig. 33, it may be concluded that results agree well in terms of surge ("XPOS") and yaw. These two quantities are primordially affected by the response induced by the mooring lines stiffness and the global rigidity of the bridge girder, which increases the confidence on the correct overall physical modelling of the truncated

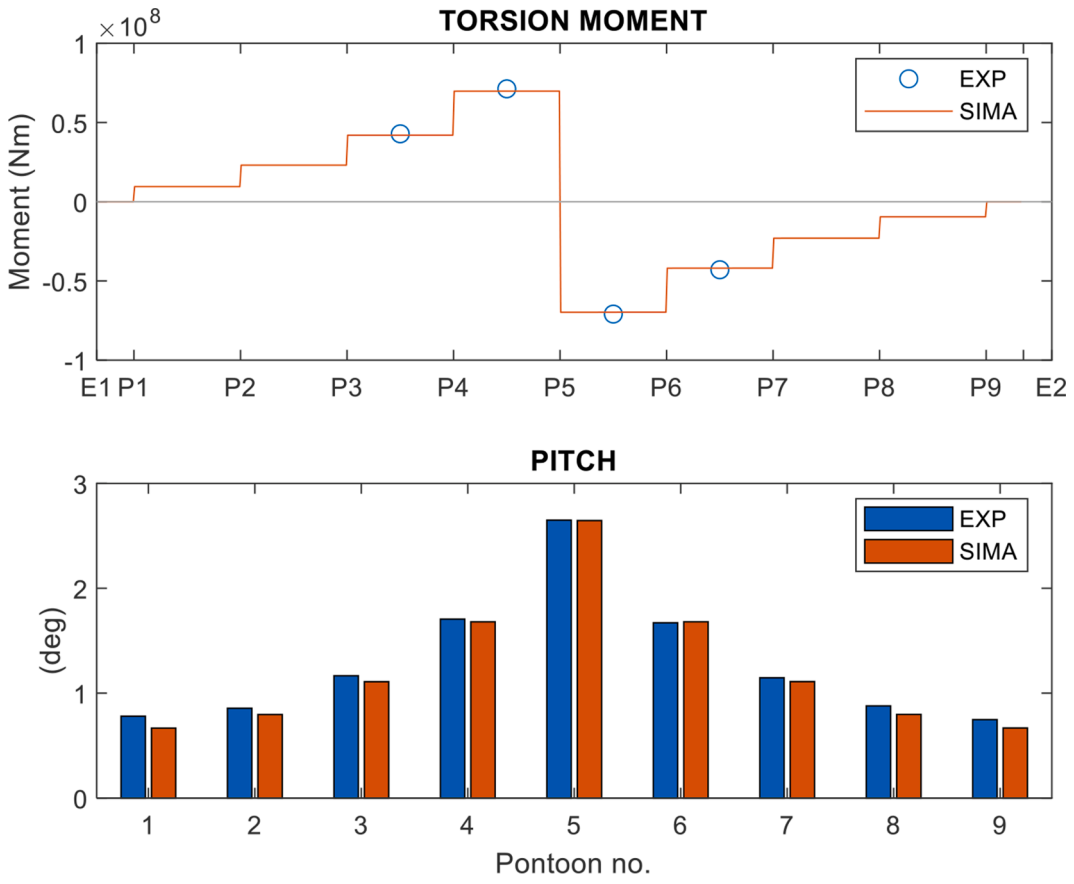

Fig. 26. Static torsion test: added 20 kg to ponton P5 with a lateral offset of 0.75m – both values in model scale; plot in full scale.

model structural properties and the scaling procedure applied. The same can also be said in terms of pitch, although the empirical response amplitude is reduced considerably at the natural frequency at approx. 6.6 s. This reduction is most surely caused by the lack of viscous damping applied in the numerical model, while the hard knuckle in the transition of the pontoons bottoms and side shells surely induces vortex shedding.

In what regards sway ("YPOS") and roll, the quantities are very small and most surely induced by parasitic reflections from the walls of the basin and other basin geometry details. However, there are clear amplifications for the pontoons other than P5 that are only somewhat predicted for P1 and P9 in the numerical simulations, regarding roll, while they are predicted to some extent for the sway in all pontoons although with slightly lower periods. On the other hand, it is important to realize that there are considerable differences in the frequency range of the RAO peak predicted by regular wave screening (same period as for the peak for surge, approx. 12.5 s) relative to the usage of the broadband wave elevations. This suggests that the usage of the Pink Noise wave system per se is of variable validity depending on the actual motions of the mode being estimated. This is not particularly surprising, as smoothing of the spectral responses involved in the RAO estimation (motion and wave elevation) is necessarily carried out, which increases uncertainty when very small responses are present.

Special attention should be given to the heave motion, where the numerical predictions follow reasonably well the experimental ones, except for a significant amplification which seems to be coupled with pitch, close to 6.3 s, and a minor one, at about 5.6-5.7 s. A speculative hypothesis for this phenomenon is the existence of positive symmetric interference wave effects arising from multi-body radiation and diffraction effects exciting this particular mode at this narrow frequency band. In fact, a period of 6.33 s, which is very close to the peaks shown in Fig. 33, corresponds to a deep-water wavelength of 62.5: half the distance between the centres of consecutive pontoons. Again, mind that hydrodynamic interaction is not present in the numerical model. Another explanation is vaguer and may be stated as the existence of a higher order pitch/heave coupling exciting resonant heave responses of the pontoons. Regarding the aforementioned minor amplification, the deep-water half-wavelength for a wave of period 5.66 s is approx. 25 m, also a divisor of the inter-pontoon spacing, leaving room for speculation on possible hydrodynamic interaction effects. An additional important aspect to consider is the clearly symmetrical nature of the motions RAOs about P5: a good indicator of the ability of the design for the connection between P9 and the land supported tripod (Fig. 7) to not induce undesirable non-negligible artificial loads.

The RAO of the bending moments at two symmetrical positions is shown in Fig. 34 for the same wave load conditions as those for Fig. 33. These results are especially relevant to verify their coherence with those of the motions' RAOS, as they are obtained from completely independent measurement systems. Regarding the torque ("TY"), the response follows the overall pattern superimposed by the roll and surge of the pontoons, the first deeming local loads, and the second the effects of the surge-to-roll coupling loads exerted by the mooring lines at the ends of the model. The vertical bending of the beam girder ("MX") clearly shows a coherent pattern with the roll and heave motions for the experimental data, showing that the two peaks shown in Fig. 33 for heave are physical. The horizontal bending moment RAO ("MZ") follows quite strictly the pattern of the surge of the pontoons, as expected. Finally, regarding the numerical results, they can be said to agree very well with empirical data in overall, except for the vertical bending moment, as anticipated from observation of Fig. 33.

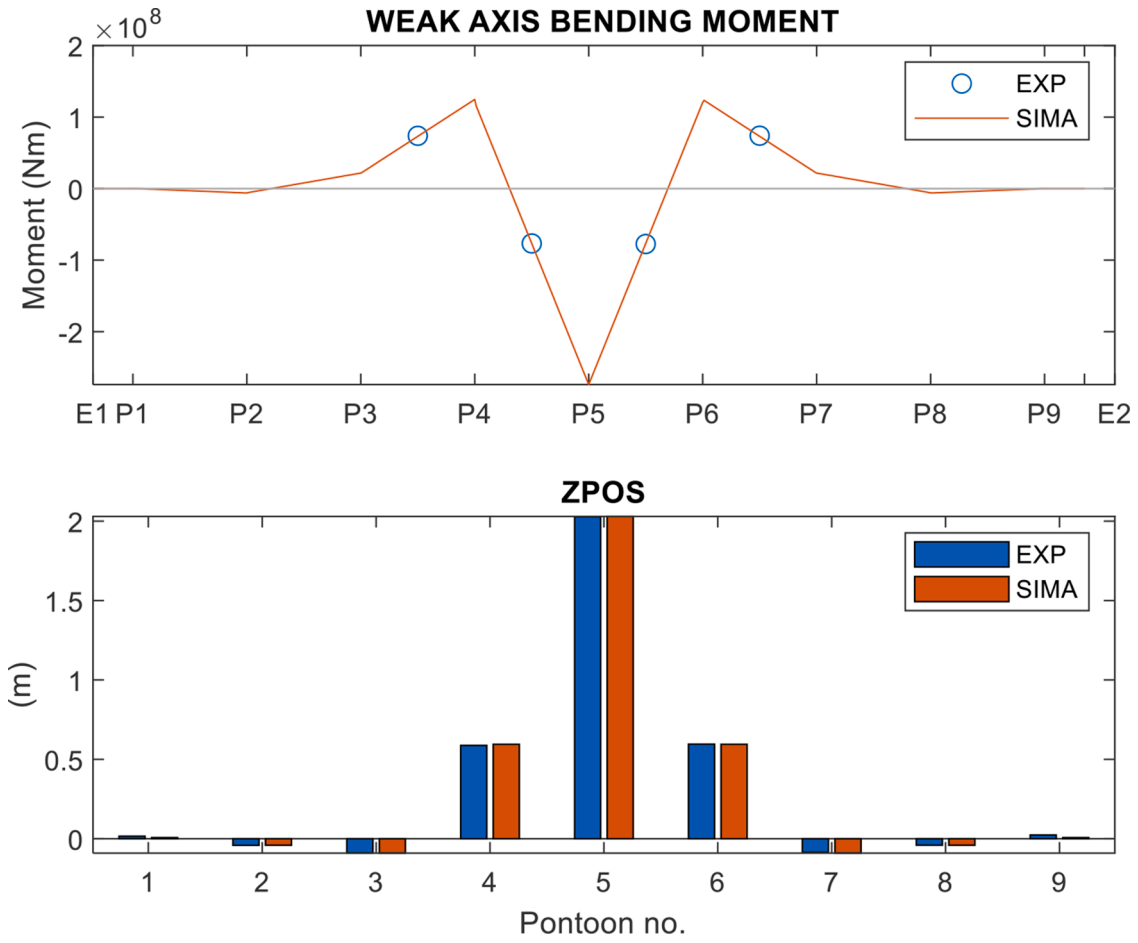

Fig. 27. Static vertical loading test: pontoon no. 5 is lifted. Values in full scale.

7. Conclusions

A literature review and presentation of the main challenges regarding physical scaled model tests for very long floating bridges has been presented. These challenges were not only acknowledged at the start but also experienced during the planning, execution, and analysis, of the model tests herein presented for a 1 km truncated segment of a floating bridge with approx. 5 km.

The procedures and rationale applied to the model test design setup have been described as well as many of the details in the experiments. Important comparisons with numerical data to assess a proper physical model of the truncated segment has been presented and results give way to the conclusion that this has been successfully achieved in overall. Some hypothesised nonlinear pitch-heave coupling phenomenon has been identified in Section 6.4, which requires further study.

The authors believe this paper will help other researchers to design and conduct their own experimental campaigns targeting large floating coastal structures, either by replicating the approach presented herein or building from it. Furthermore, a subset of experimental results is openly shared with the community in the expectation that such dataset can be of relevance for benchmarking numerical simulations. To the best of the authors' knowledge, the work presented herein is pioneer, at least considering published material available to the scientific community, in the sense that it includes a methodological design process for a truncated model experimental test setup of a very large floating structure from the starting point of the full structure without a priori considerations.

A succinct set of recommendations for model tests of large floating structures can be made based on the experience gained in the work herein described:

1 Overall approach to carry out model tests of LFCS: The problem with performing hydrodynamic scaled physical model tests of LFCS's is the very large extension of these structures, leading to problems in tank testing: (1) to achieve high quality environment generation; (2) hydrodynamic quantities' scaling issues for too small scales; (3) quality of the model production; (4) quality of the measurements. A recommended option is to carry out experiments to validate and calibrate key truncated segments of the full structure under relevant environmental loads, the conclusions from a posterior exploitation of the results can then be extrapolated to a numerical model of the full structure validation. The test matrix in terms of environmental load cases should be defined a priori based on outputs of dedicated environmental assessment at the deployment site and a preliminary numerical study of the responses of the structure.

2 Scale considerations: To start the experimental setup design process, a recommended strategy is to first investigate the feasible scale range for wave generation (and current generation, if relevant) in the basin considering the design load cases to be tested. A possible feasible scale definition can be one which, for each of the environmental load cases, complies with the following conditions:
- Target current able to be generated (if present in the test matrix).
- Wave-makers' limits, e.g., amplitude, velocity and acceleration, are not exceeded.
- Less than 5% of the energy in the wave spectrum tail is cut off.
- All spectral ordinates in excess of 10% of the spectral peak are modelled.
- Significant wave heights are higher than 2 cm in model scale.
- Empirical/high fidelity numerical results from the basin database of wave generation show the feasibility of the targeted sea states

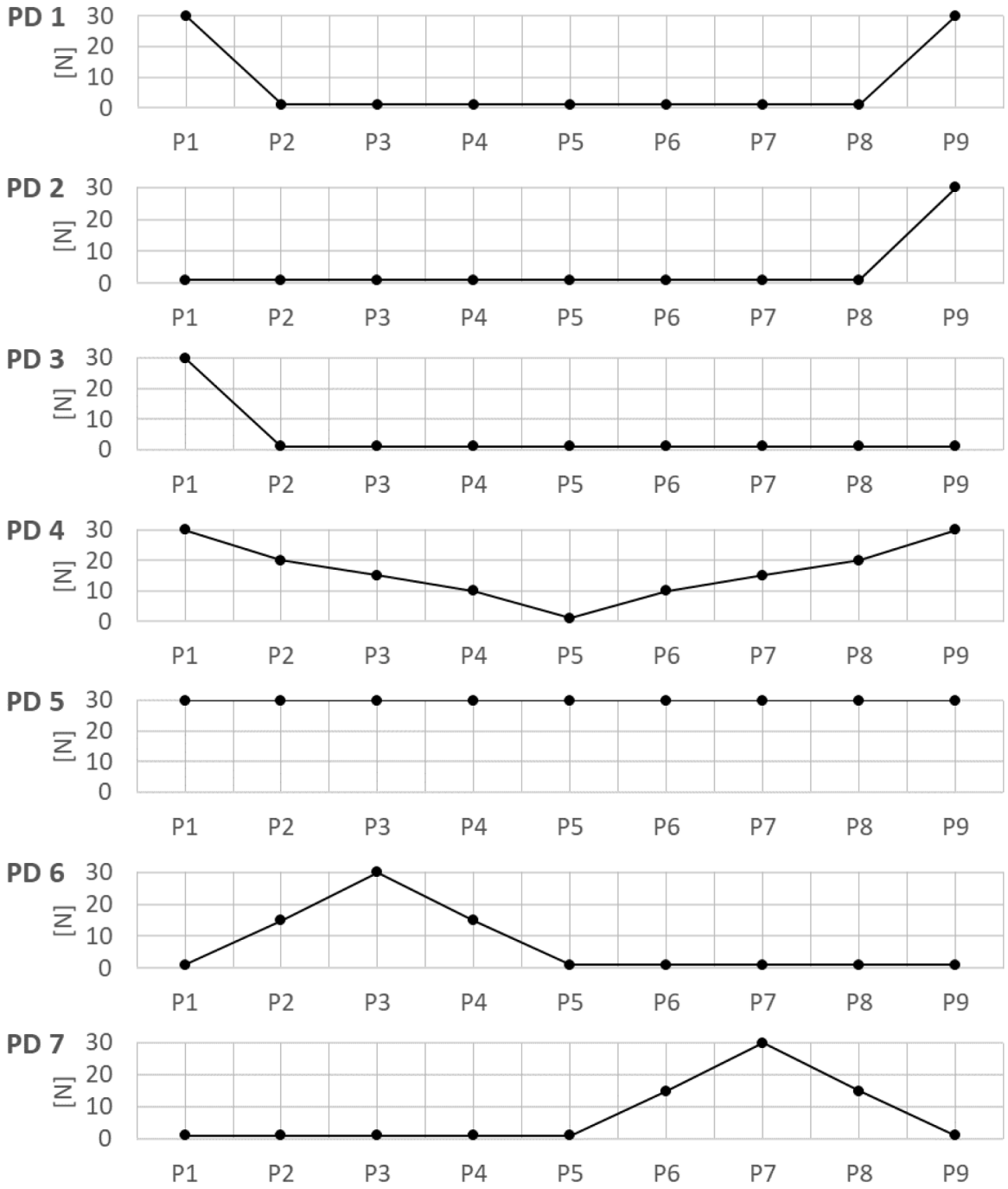

Fig. 28. Pull-out and decay initial applied forces (model scale).

considering: (a) Lower frequency limits; (b) Good homogeneity of the wave field and current across the length of the LFCS; (c) Alternative to (b), is to have a very good documentation of observed inhomogeneities e.g. using wave probe arrays at each floating body location and implementing a numerical scheme to handle arbitrary inhomogeneous wave fields as described in Rodrigues (2021).

- Mind that relevant wave conditions will likely be in the form of combinations of wind sea and swell, with very different wave period ranges that will probably make it unfeasible to generate both types of sea states. On the other hand, low frequency drift forces arising from wind seas may be generated to excite responses in the swell frequency region.
- Applying the above conditions for the targeted long crested wind seas, will define the smallest feasible scale from the point of view of wave generation. Factors such as current and wave elevation control and their accurate documentation across the basin need to be considered in addition to conclude on the largest possible scale.

3 **Generation of environmental conditions:**

- **Short-crested seas:** Testing for short-crested seas is particularly challenging due to the large extent of the model and the typical very high spreading of the sea states at the locations of interest. Achieving a full coverage of all the wave components in all parts of the model is then extremely difficult. It is important to realize that positioning the model parallel to a multi-flap wave maker to increase the wave coverage is limited by a necessary clearance to avoid excitations from the flaps' evanescent waves and increased

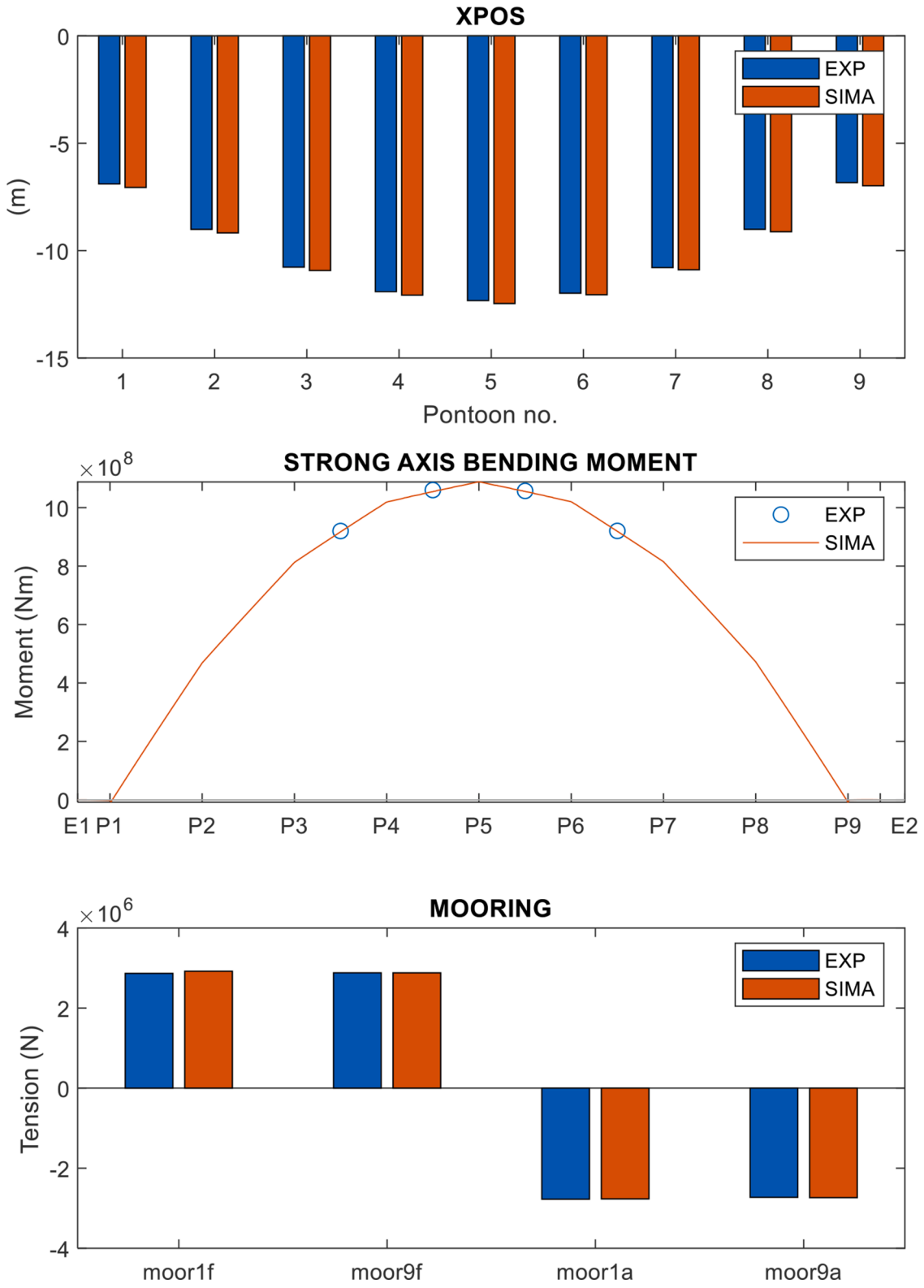

Fig. 29. Static lateral loading test: all pontoons pulled laterally with an applied force of 30 N on each – both values in model scale; plot in full scale.

wall effects, and possibly (depends on the actual system used) ensure a good coverage of motion capture systems without the need to use an excessive number of cameras. It is recommended that short-crested seas be limited if found relevant under a numerical modelling-based design and verification approach, or directionally narrowed in the experimental campaign, if necessary, as opposed to considering very small models. If the option is for narrowing the sea state, then attention should be given to the fact that wave energy becomes directionally concentrated which may lead to dramatic increases or the response of the structure especially for mean wave headings perpendicular to the bridge.

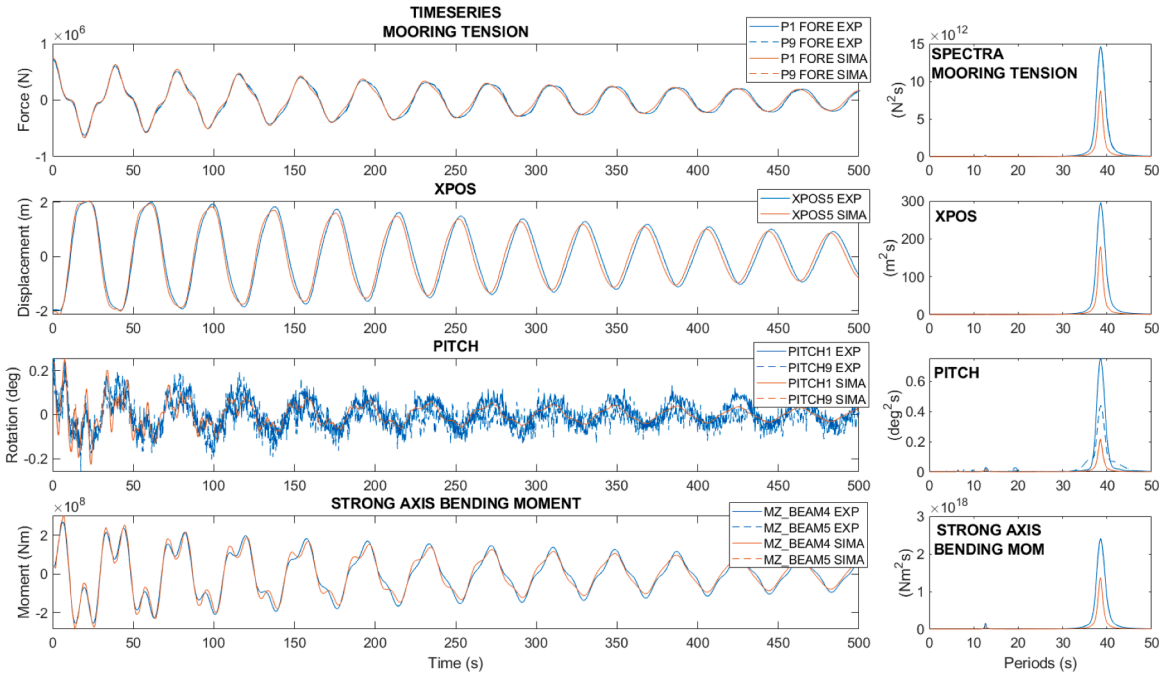

Fig. 30. Decay response to initial condition PD 1 (full scale).

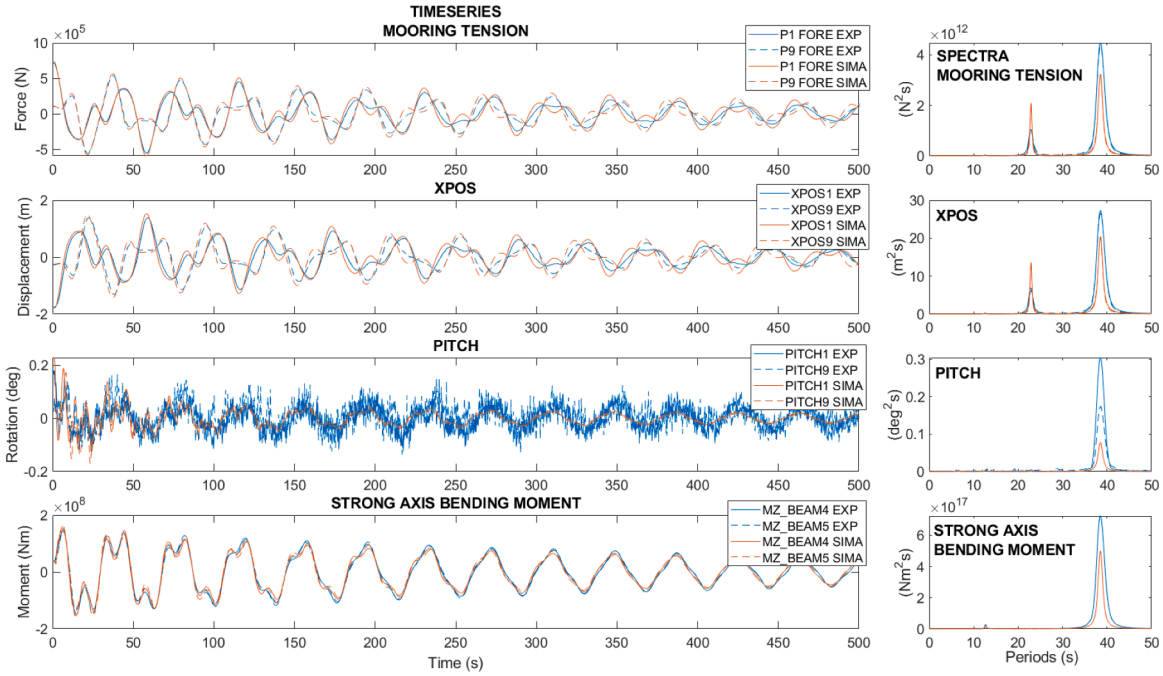

Fig. 31. Decay response to initial condition PD 3 (full scale).

- **Wind modelling:** Including wind induced forces on the structure throughout its span is challenging, not only due to the large area than needs to be covered and the prospective inhomogeneity of the wind field along the structure. Physical generation of wind through fans applied to the model raises issues relating to different scaling approaches – Froude scaling is typically used for wave induced hydrodynamics, while Reynolds scaling is advised for the wind forces. The option for forcing the model at discretized points in the model through application of pre-generated wind forces from simulations, through pulling cables controlled by winches, seems to be a promising efficient approach with the ability to also be used for documentation tests (see point 5 below). Fitting the model with small fans distributed through the model at relevant points is also an option. Naturally, as denser the application points' array is and as more sophisticated the fans/actuators are the better. An actuator setup able to induce forces and moments at each location at both sides of the model should be ideal. Preliminary simulations to compare the responses of the model to wind with a turbulence model applied and with the forces induced by the cables with the perspective discretization should be carried out.

  Another point worth mentioning is that, as for the hydrodynamic problem, one may argue that there is also a need to validate the

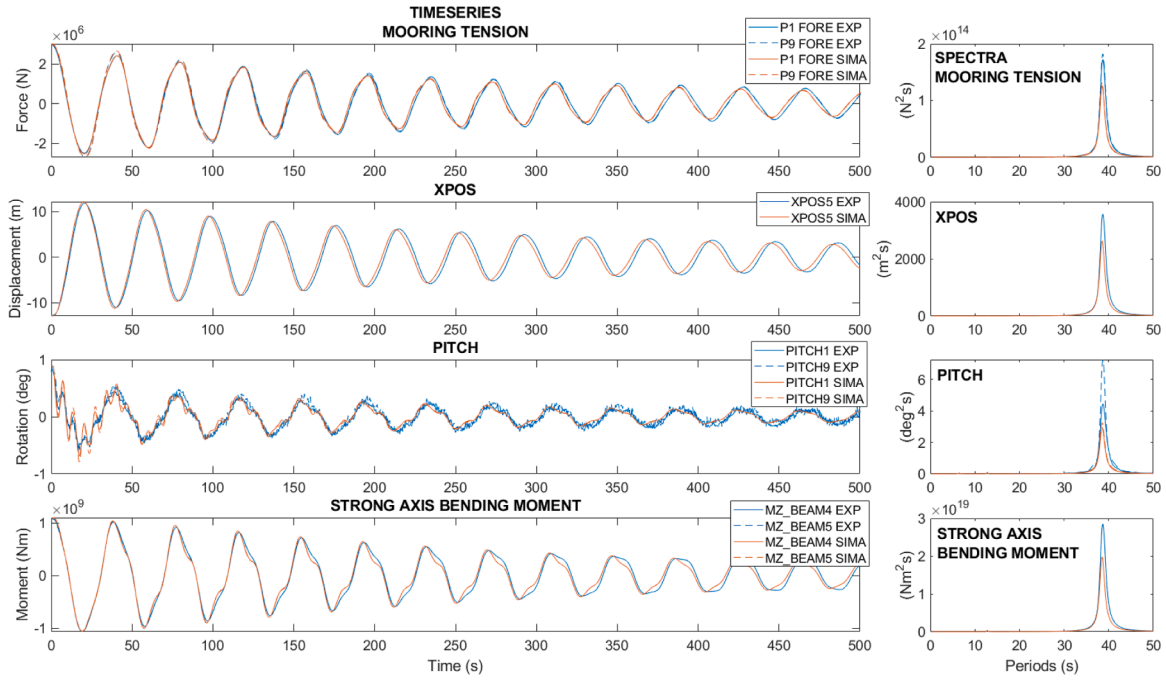

Fig. 32. Decay response to initial condition PD 5 (full scale).

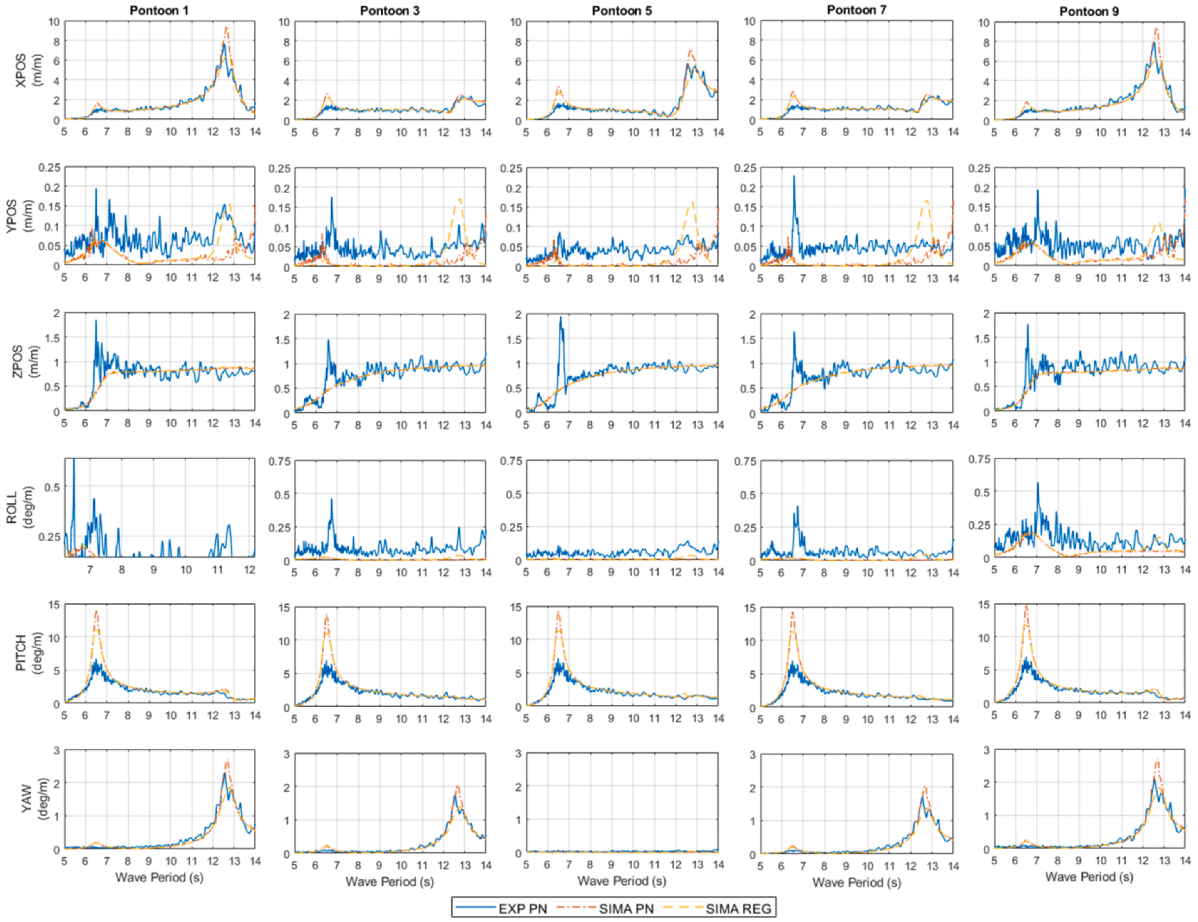

Fig. 33. Full scale motion response amplitude operators (RAO) for waves perpendicular to the bridge girder (wave heading 0deg and model position A). "EXP PN" and "SIMA PN" stand for estimates obtained from broadband wave runs obtained experimentally and numerically, respectively. "SIMA REG" is obtained from individual numerical simulations using an array of wave frequencies.

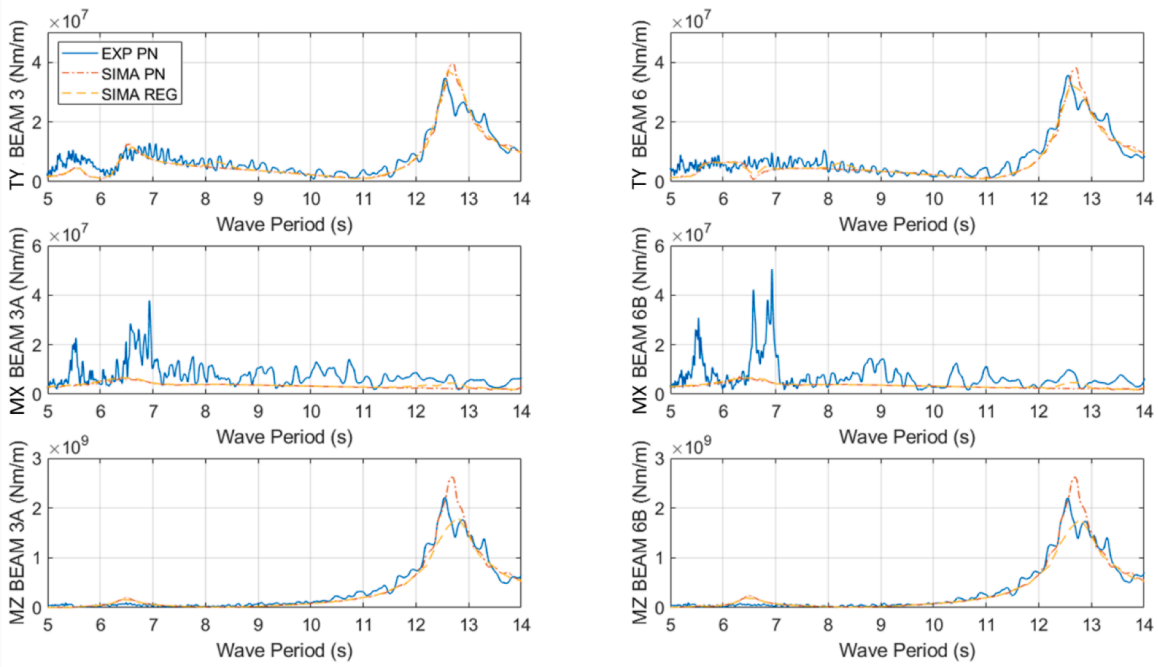

Fig. 34. Full scale torque ("TY") and Bending moments ("MX" and "MZ") response amplitude operators (RAO) for waves perpendicular to the bridge girder (wave heading 0 deg and model position A). "EXP PN" and "SIMA PN" stand for estimates obtained from broadband wave runs obtained experimentally and numerically, respectively. "SIMA REG" is obtained from individual numerical simulations using an array of wave frequencies.

simulated wind forces on the model. This can be done with wind tunnel tests, although special challenges arise as well. Without going deep on the wind modelling, which is out of scope of this communication, two difficulties seem evident: (1) similar issues regarding the length of the full structure, which will be too large for appropriate scales for good measurements and wind flow modelling, then probably requiring truncation with its specific challenges; (2) A possible influence of the wave height on the wind force regime as the gap between the structure and the water surface (e.g. for the floating bridge herein described, this would be the gap between the water and the lower face of the bridge deck) varies, leading to possible dangerous phenomena.

- **Prescribed wave inhomogeneity:** To the best of the authors' knowledge, practical generation of arbitrary inhomogeneous seastates in a standard basin (non-circular) has no published established procedure. Adding bathymetric variations on the basin, therefore inducing shoaling effects (Wang et al., 2015), is a possible approach, however probably economically inefficient in most cases. This is an important open question, as environmental loads inhomogeneity is deemed as an important effect on extreme dynamic response of extended bridge structures and may actually be accounted for in numerical simulations, e.g., resorting to direct matrix methods as in Rodrigues (2021).

4 **Boundary conditions of truncated model:** Ideally, active boundary conditions using sophisticated actuators governed by a numerical simulation running the response of the missing part of the structure are in place. This scheme is in fact a software in the loop approach. However, a problem with this approach is that the simulated part of the model behaves according to parameters that have not been experimentally validated. One can speculate that sophisticated machine learning based algorithms may govern the active boundary conditions, then replacing the simulated missing section of the structure. The training of the algorithm could be achieved from running a sufficient number of simulations and could inclusively also be enhanced from the empirical data acquired during the experiments. However, there is a lot of speculation to this, for the technical challenges foreseen seem to be dauting.

On the other hand, passive boundary conditions are in line with the current state of the art of model testing. However, the challenge here is the choice of what condition to apply. As the response of the structure in terms of comparison of the flexural response modes, at least for the case of a floating bridge presented herein, depends not only on the boundary condition (clamped, cantilever, free, hybrid) but also on the actual environmental load applied, the choice is far from obvious. Typically, one mode may be targeted, but then the remaining ones are not controlled. A possible recommendation is for the researcher to first have it very clear what is the dominant mode that is to be modelled, and then carry out a considerable preliminary simulation based spiral study to converge to a final experimental setup.

5 **Experimental system documentation:** Documentation and validation of the experimental setup is a crucial step to ensure that the empirical data is meaningful. For hydroelastic models, tests should be carried to document the static stiffness properties of the structural elements and validate them against the target modelled properties, both of its individual components, prior to the deployment of the model in the basin, and of its global behaviour at the onset of the test campaign with the model fully assembled and floating. The dynamic properties need also to be documented as much as feasible during the experimental campaign. The approach of using actuator winches to force the model to deform into prescribed shapes by pulling cables attached to the model at a discrete distribution of points along the model seems to be a solution to achieve this efficiently, allowing to cover a wide range of conditions involving inhomogeneous applied loads. If the winch system is able to follow the model without applying forces upon realization of decay tests, then the procedure is both efficient and accurate, allowing for multiple configurations and repetitions which would be prohibitive if done manually.

Funding

This work was supported by the Research Council of Norway through the project 268403/O80 Design and Verification of Large Floating Coastal Structures - Environmental description, structural loads,

responses and mooring system.

Availability of data and material

all relevant data in the experiments is publicly available at: Mendeley data (https://data.mendeley.com/datasets/z4fnc85g3y/1).

Code availability

N/A.

Declaration of Competing Interest

The authors declare that they have no known competing financial interests or personal relationships that could have appeared to influence the work reported in this paper.

Acknowledgement

This work was supported by the Research Council of Norway through the project 268403/O80 Design and Verification of Large Floating Coastal Structures - Environmental description, structural loads, responses and mooring system.

References

Abrahamsen, B.C., Stansberg, C.T., 2019. LFCS Review report – Model testing model testing of large structures in a wave basin. URL http://hdl.handle.net/11250/2603349 (accessed 07.06.2022).

Cheng, Y., Ji, C., Zhai, G., Gaidai, O., 2016. Hydroelastic analysis of oblique irregular waves with a pontoon-type VLFS edged with dual inclined perforated plates. Mar. Struct. 49, 31–57. https://doi.org/10.1016/J.MARSTRUC.2016.05.008.

Cheng, Z., Gao, Z., Moan, T., 2018. Wave load effect analysis of a floating bridge in a fjord considering inhomogeneous wave conditions. Eng. Struct. 163, 197–214. https://doi.org/10.1016/J.ENGSTRUCT.2018.02.066.

DNV-GL, Dnv-rp-c205, environmental conditions and environmental loads. Recommended practice, 2017.

Fonseca, N., Ren, N., Chi, Z., Hellan, O., Rodrigues, J.M., Magee, A.R., 2019. Hydrodynamic model tests with a large floating hydrocarbon storage facility. In: Proceedings of the International Conference on Offshore Mechanics and Arctic Engineering - OMAE 6. https://doi.org/10.1115/OMAE2019-96761.

Giske, F.I.G., Kvåle, K.A., Leira, B.J., Øiseth, O., 2018. Long-term extreme response analysis of a long-span pontoon bridge. Mar. Struct. 58, 154–171. https://doi.org/10.1016/J.MARSTRUC.2017.11.010.

Kagemoto, H., Fujino, M., Murai, M., 1998. Theoretical and experimental predictions of the hydroelastic response of a very large floating structure in waves. Appl. Ocean Res. 20, 135–144. https://doi.org/10.1016/S0141-1187(98)00017-0.

Kvåle K.A., 2017. Dynamic behaviour of floating bridges exposed to wave excitation: a numerical and experimental investigation (PhD thesis). URL http://hdl.handle.net/11250/2479175 (accessed 07.06.2022).

Moan, T., Eidem, M.E., 2020. Floating bridges and submerged tunnels in Norway—the history and future outlook. Lect. Notes Civ. Eng. 41, 81–111. https://doi.org/10.1007/978-981-13-8743-2_5.

MARIN, 2020. MARIN tested SPACE@SEA floating mega island [WWW Document]. https://www.marin.nl/en/news/marin-tested-spacesea-floating-mega-island. (accessed 07.06.2022).

Ohmatsu, S., 2005. Overview: research on wave loading and responses of VLFS. Mar. Struct. 18, 149–168. https://doi.org/10.1016/J.MARSTRUC.2005.07.004.

Multiconsult, 2017. SBJ-31-C3-MUL-22-RE-100-0 - Analysis and design (Base Case). Multiconsult AS: Oslo, Norway. URL https://www.vegvesen.no/globalassets/vegprosjekter/utbygging/e39stordos/vedlegg/sbj-31-c3-mul-22-re-100-0-analysis-and-design-base-case.pdf (accessed 07.06.2022).

Nwogu, O., 1989. Maximum-entropy estimation of directional wave spectra from an array of wave probes. Appl. Ocean Res. 11 (4), 176–182. https://doi.org/10.1016/0141-1187(89)90016-3.

Rodrigues, J.M., 2022. Dataset from model tests of a hydroelastic truncated floating bridge - SINTEF Ocean. Mendeley Data. https://doi.org/10.17632/z4fnc85g3y.1 (draft) [WWW Document]URL, 1. https://data.mendeley.com/datasets/z4fnc85g3y/1. (Accessed 8 June 2022). accessed 08.06.2022.

Rodrigues, J.M., 2021. A procedure to calculate first-order wave-structure interaction loads in wave farms and other multi-body structures subjected to inhomogeneous waves. Energies 14, 1761. https://doi.org/10.3390/EN14061761, 2021Page141761.

ORCINA, 2021. OrcaFlex [WWW Document]. https://www.orcina.com/orcaflex/. (accessed 07.06.2022).

Rodrigues, J.M., Økland, O., Fonseca, N., Leira, B., Alsos, H.S., Abrahamsen, B.C., Aksnes, V., Lie, H., 2020. Design and Verification of Large Floating Coastal Structures: Floating Bridges for Fjord Crossings. Paper presented at the The 30th International Ocean and Polar Engineering Conference, Virtual, October 2020.

SINTEF Ocean, 2021. SIMA [WWW Document]. https://www.sintef.no/en/software/sima/. (accessed 07.06.2022).

SINTEF Ocean, 2017. Large Floating Coastal Structures (LFCS) [WWW Document]. https://www.sintef.no/projectweb/lfcs/.

Song, H., Cui, W., Tao, L., Liu, Y., 2008. Hydroelastic response of VLFS on uneven sea bottom. In: Proceedings of the International Conference on Offshore Mechanics and Arctic Engineering - OMAE, 2, pp. 433–443. https://doi.org/10.1115/OMAE2005-67557.

Stansberg, C.T., 1996. Motions of large floating structures moored in irregular waves: experimental studies. In: Proceedings of the Workshop on Very Large Floating Structures (VLFS '96). Hayama, Japan.

Stansberg, C.T., Tørum, A., Næss, S., 1990. On a model study of a box type floating breakwater. Wave damping and mooring forces. In: Proceedings of the 27th PIANC Congress. Osaka, Japan.

Statens vegvesen, 2018. SBJ-32-C3-SVV-90-BA-002 Design Basis Bjørnafjorden Rev E.

Statens vegvesen, 2017. Bjørnafjorden, straight floating bridge phase 3 - Analysis and design (Base Case) - - Doc no. SBJ-31-C3-MUL-22-RE-100.

Tucker, M.J., Challenor, P.G., Carter, D.J.T., 1984. Numerical simulation of a random sea: a common error and its effect upon wave group statistics. Appl. Ocean Res. 6, 118–122. https://doi.org/10.1016/0141-1187(84)90050-6.

Viuff, T., Leira, B.J., Xiang, X., Øiseth, O., 2019. Effects of wave directionality on extreme response for a long end-anchored floating bridge. Appl. Ocean Res. 90, 101843 https://doi.org/10.1016/J.APOR.2019.05.028.

Viuff, T., Xiang, X., Øiseth, O., Leira, B.J., 2020. Model uncertainty assessment for wave- and current-induced global response of a curved floating pontoon bridge. Appl. Ocean Res. 105, 102368 https://doi.org/10.1016/J.APOR.2020.102368.

Wang, Z., Zhang, P., Nie, X., Zhang, Y., 2015. Manipulating water wave propagation via gradient index media. Sci. Rep. 5, 1–9. https://doi.org/10.1038/srep16846, 201515.

Xiang, X., Løken, A., 2019. Aspects of hydrodynamic loading and response in design of floating bridges. In: Proceedings of the Asme 38th International Conference on Ocean, p. 9. Offshore and Arctic Engineering.

Xiang, Xu, Løken, A., 2019. Hydroelastic analysis and validation of an end-anchored floating bridge under wave and current loads. In: Proceedings of the International Conference on Offshore Mechanics and Arctic Engineering - OMAE 9. https://doi.org/10.1115/OMAE2019-95114.

Yoon, J.S., Cho, S.P., Jiwinangun, R.G., Lee, P.S., 2014. Hydroelastic analysis of floating plates with multiple hinge connections in regular waves. Mar. Struct. 36, 65–87. https://doi.org/10.1016/J.MARSTRUC.2014.02.002.

Young, W.C., Budynas, R.G., Sadegh, A., 2012. Roark's Formulas for Stress and Strain, 8th ed., p. 1072